Journal of Nuclear Materials 619 (2026) 156244

Contents lists available at ScienceDirect

Journal of Nuclear Materials

journal homepage: www.elsevier.com/locate/jnucmat

A thermodynamic study of fluorite/bixbyite equilibria in the UO_2–$PuO_{1.5}$–PuO_2 system

Victor L. Vinograd [a,*], Romain Vauchy [b]

[a] Institute of Fusion Energy and Nuclear Waste Management. Nuclear Waste Management (IFN-2), Forschungszentrum Jülich GmbH, Jülich, Germany
[b] MOX Fuel Development Department. Japan Atomic Energy Agency, 4-33 Muramatsu, Tokai-Mura, Ibaraki 319-1194, Japan

HIGHLIGHTS

- Five-endmember (UO_2, PuO_2, $PuO_{1.5}$, $Pu_{0.25}Pu_{0.75}O_{1.625}$ and $U_{0.25}Pu_{0.75}O_{1.625}$) thermodynamic models of the fluorite and bixbyite solid solutions are developed and applied to simulate phase equilibria in the UO_2–$PuO_{1.5}$–PuO_2 system at different Pu/(Pu + U) ratios.
- The cubic lattice parameters of the fluorite and bixbyite phases are modelled with an ion-packing approach, consistently with the thermodynamically constrained fractions of the five endmembers.
- The cubic lattice parameters are plotted as functions of the temperature or *O/M* ratio, allowing a direct fitting of the model to relevant experimental data.
- The results of the modelling suggest that Pu/(Pu + U) ratios in fluorite, bixbyite, and in the rhombohedral phase remain the same at temperatures below ~1000 K, i.e., no inter-phase U/Pu- partitioning occurs despite complex exsolution phenomena within fluorite and bixbyite.

GRAPHICAL ABSTRACT

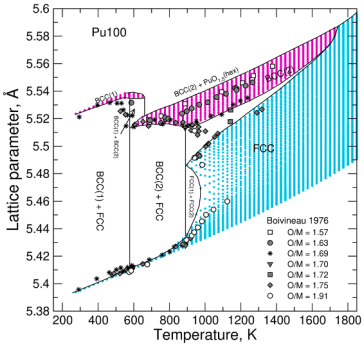

ARTICLE INFO

Keywords:
Pu-doped UO_2
MOX fuel
Nuclear fuel
Miscibility gap
BCC and FCC solid solutions

ABSTRACT

Thermodynamic properties of $U_{1-z}Pu_zO_{2+\delta}$ fluorite (FCC) and $U_{1-z}Pu_zO_{2+\delta}$ bixbyite (BCC) in the UO_2–$PuO_{1.5}$–PuO_2 system are assessed by considering phase equilibrium constraints and data on the variation of oxygen to metal ratio (*O/M*) as a function of the chemical potential of O_2. Thermodynamically, both BCC and FCC are described as ordered solid solutions allowing for a decrease in the configurational entropy of their oxygen/vacancy distributions at the specific values of $\delta = -0.5$ and $\delta = -0.375$ ($O/M = 1.5$ and $O/M = 1.625$). With this approach, fluorite/bixbyite equilibria in $PuO_{1.5}$–PuO_2 and in UO_2–$PuO_{1.5}$–PuO_2 are reproduced well with little effort. Moreover, we show that a large manifold of experimental data on the UO_2–$PuO_{1.5}$–PuO_2 system is consistent with the assumption that Pu/(Pu + U) ratios in individual phases remain equal to the total Pu/(Pu + U) ratio in the system, i.e., phase equilibration does not involve inter-phase U/Pu-partitioning.

* Corresponding author.
E-mail address: v.vinograd@fz-juelich.de (V.L. Vinograd).

https://doi.org/10.1016/j.jnucmat.2025.156244
Received 1 July 2025; Received in revised form 15 October 2025; Accepted 22 October 2025
Available online 25 October 2025

1. Introduction

Uranium-plutonium mixed oxides (MOX) assemblies are often added to Light Water Reactor cores and are discussed as prospective fuels for Generation IV Fast Neutron Reactors [1]. The average plutonium content of LWR and FNR fuels typically ranges between 4∼11 mol % and 25∼35 mol %, respectively. FNR fuels typically exhibit a homogeneous cation distribution [2], whereas LWR fuels, often produced by the so-called MIMAS process, show considerable inhomogeneity revealed as PuO_2-rich agglomerates embedded in UO_2-rich matrix [3]. Understanding phase relations in the UO_2–$PuO_{1.5}$–PuO_2 system is important for optimizing MOX synthesis and reprocessing, for both LWR and FNR applications. It is also essential for accurately capturing thermophysical behavior of MOX fuels under operational or accidental conditions. Moreover, the UO_2–$PuO_{1.5}$–PuO_2 system serves as a foundation for a number of chemically more complex systems, e.g., for systems containing Am and Np, that are important for optimizing synthesis conditions and thermophysical properties of transmutation matrices for minor actinides [4,5]. Thermodynamic modelling of such systems is hindered by unsolved problems in the description of UO_2–$PuO_{1.5}$–PuO_2.

Phase equilibria in UO_2–$PuO_{1.5}$–PuO_2 are characterized by a remarkable complexity that is primarily revealed in a peculiar coexistence of FCC and BCC phases. The recent CALPHAD assessment by Guéneau et al. [6] provided a comprehensive description of FCC/BCC phase relations in the pure $PuO_{1.5}$–PuO_2 system. However, a similarly detailed representation of FCC/BCC equilibria in UO_2–$PuO_{1.5}$–PuO_2 is yet to be achieved. The problem identified in [6] is the lack of thermodynamic constraints for the UO_2-bearing BCC phase. Here we try to overcome this problem. We show that the lack of data can be compensated by a guess that the thermodynamic mixing properties of BCC and FCC are similar, with the exception that the oxygen-vacancy sublattice in BCC is more strongly ordered than in FCC. We then show that by starting with the same models for FCC and BCC and by tuning the Gibbs free energies of endmembers in BCC in the direction of a higher degree of oxygen/vacancy ordering, it appears possible to closely reproduce experimental phase boundaries. We also show that the manifold of data suitable for constraining thermodynamic properties of BCC and FCC can be significantly enlarged by linking the thermodynamic model to an ion-packing model, with which lattice parameters of fluorite-like phases can be computed as functions of thermodynamic model parameters. With such a combined structural-thermodynamic model, the lattice parameters of cubic phases that are typically provided in most experimental studies could be directly used in the thermodynamic assessment as experimental constraints. Because such a model cannot yet be implemented within popular thermodynamic software packages, we develop new modelling tools and our own task-related thermodynamic data set. Consequently, this effort should be considered parallel and complementary to well-established CALPHAD-type assessments.

The ordering in BCC at O/M ∼1.625 has been proposed in a study of Sari et al. [7] as a hypothesis explaining the low-temperature termination point of the so-called "1.61" BCC phase in the $PuO_{1.5}$–PuO_2 system [7]. We start by reviewing the main features of known phase diagrams of $PuO_{1.5}$–PuO_2 and UO_2–$PuO_{1.5}$–PuO_2 systems, emphasizing remaining uncertainties and inconsistencies. After this, we introduce thermodynamic models for relevant phases and outline the fitting procedure. Then, we present results of the modelling as T vs. O/M and a vs. T diagrams (a is the lattice parameter) computed at certain fixed values of Pu/(Pu + U), as well as O/M vs. Pu/(Pu + U) and a vs. Pu/(Pu + U) diagrams computed at different temperatures. Finally, we discuss the results and propose items for further research.

1.1. Phase relations in $PuO_{1.5}$–PuO_2

Despite much experimental and modelling effort, the phase relations in $PuO_{1.5}$–PuO_2 remain partially uncertain. Experimental problems include high radioactive activities (or small sizes) of samples, the ease of their spontaneous oxidation and difficulties in distinguishing superlattice reflections in X-ray diffraction patterns. Theoretical problems are related to the lack of thermodynamic models able to describe the complexity of chemical composition and of ordering phenomena revealed by BCC and FCC. The assessment of Guéneau et al. [6] essentially confirmed the diagram of Wriedt [8] for $PuO_{1.5}$–PuO_2 system, which has been constructed as a synthesis of earlier experimental studies [7,9–13]. The T vs. X(O) diagram of Guéneau et al. [6] is redrawn in Fig. 1 as T vs. O/M plot. The diagram shows that at ambient temperature, BCC with the stoichiometry of ∼1.52 (α-Pu_2O_3, here designated BCC(1)) coexists with an almost stoichiometric FCC $PuO_{2+\delta}$ fluorite with $\delta \sim 0$ (here FCC(1)). At ∼600 K, these two phases react, producing another BCC phase (BCC(2)) with O/M of ∼1.61. At $T > 600$ K BCC(2) coexists with FCC(1). The homogeneity range of BCC(2) expands with increasing temperature to a larger O/M reaching O/M ∼1.71 at ∼900 K. At about this temperature, BCC(2) reacts with FCC(1) forming another FCC phase (FCC(2)) with the composition of O/M ∼1.75 and the triple association of BCC(2) + FCC(1) + FCC(2) is formed. Above this temperature, the triple point terminates, giving rise to two-phase fields; at $O/M < 1.75$ BCC(2) coexists with FCC along a two-phase loop, while at $O/M > 1.75$ FCC(1) coexists with FCC(2). The FCC(1) + FCC(2) gap closes at ∼1000 K, and above this temperature, a large single-phase FCC field exists. The BCC(2) + FCC loop envelops the field of stability of BCC (2). The BCC terminates at ∼1400 K, transforming into FCC.

The low-oxygen side of the $PuO_{1.5}$–PuO_2 system is affected by the stability of the hexagonal β-Pu_2O_3. According to Wriedt [8], β-Pu_2O_3 coexists with the "1.52" BCC phase at $T < 720$ K, while at $T > 720$ K it coexists with the "1.61" BCC phase. At temperatures within the 1800 K $< T <$ 2200 K interval, the hexagonal phase is in equilibrium with the FCC fluorite [14]. In a narrow interval of 600 K $< T <$ 720 K, the "1.52" and "1.61" BCC phases coexist. The relationship between β-Pu_2O_3 (O/M = 1.5) and α-Pu_2O_3 ("1.52") at ambient temperature is less certain. In the diagrams of Gardner et al. [10], Sari et al. [7], Wriedt [8], and Guéneau et al. [6], the β-Pu_2O_3 and "1.52" phases are considered as constant composition (line) compounds, and a narrow two-phase field (β-Pu_2O_3 + α-Pu_2O_3) is drawn from ∼750 K down to 298 K.

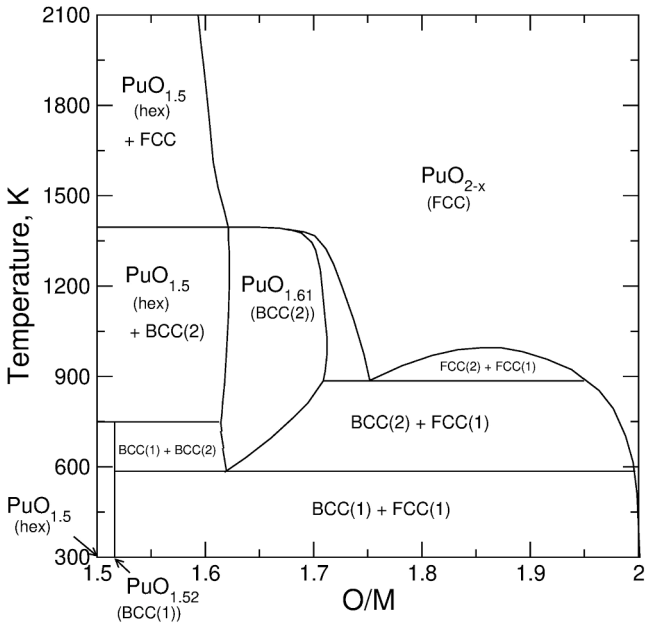

Fig. 1. Phase relations in $PuO_{1.5}$–PuO_2 system assessed with the CALPHAD method. The diagram is redrawn from Guéneau et al. [6] as a T vs. O/M plot.

1.2. Phase relations in UO_2–$PuO_{1.5}$–PuO_2

Phase relations in the UO_2–$PuO_{1.5}$–PuO_2 system are similarly governed by a coexistence of BCC and FCC phases. According to the experimental study of Sari et al. [11], the homogeneous FCC solid solution exists at ambient temperature only up to $z = Pu/(Pu + U) \sim 0.2$. At higher z values, FCC separates into two FCC phases with drastically different O/M ratios; the oxygen-rich phase with $O/M \sim 2.0$ extending from UO_2 to PuO_2, and the reduced phase with $O/M \sim 2.0 - 0.5z$ extending from UO_2 to $PuO_{1.5}$. At about $Pu/(Pu + U) \sim 0.45$ the reduced FCC phase transforms into similarly reduced BCC, while the BCC phase coexists with the oxidized FCC up to $Pu/(Pu + U) \sim 1.0$. The phase relations become more complex within the interval of $0.97 < z \leq 1.0$, where the hexagonal β-Pu_2O_3 might form. The study of Dean et al. [15] confirmed the results of Sari et al [11], and suggested that the BCC phase is stable in a reduced form, i.e., in equilibrium with graphite or Pu/U metal, over a slightly wider interval, down to $Pu/(Pu + U) \sim 0.3$. The separation into the oxygen-rich and oxygen-poor phases is well reproduced in the study of Guéneau [6], however, the FCC/BCC transition at $Pu/(Pu + U) \sim 0.45$ is not described. In Fig. 2 the X(O) vs. X(Pu) diagram of Guéneau [6] at 473 K is redrawn as an O/M vs. $Pu/(Pu + U)$ plot. According to this diagram the stability of the low-oxygen FCC phase extends up to $z \sim 0.88$, above which the triple association of two FCC phases with the BCC(1) with the composition of $PuO_{1.52}$ is formed. The relationship between FCC and BCC within the transition region of ~0.45 < $Pu/(Pu + U)$ < ~0.54 was not outlined in detail in any of the previous studies. Sari et al. [11], as well as Truphémus et al. [16], noted that this interval must be characterized by a coexistence of two FCC phases with BCC. The ternary equilibrium was indeed observed at $Pu/(Pu + U) =$ 0.46, 0.54, and 0.62 [16], however, the composition of the BCC phase was found to lie between the compositions of FCC(1) and FCC(2) phases, suggesting a non-equilibrium effect. The FCC(1) + FCC(2) equilibrium at the compositions of $U_{0.58}Pu_{0.42}O_{2+\delta}$ and $U_{0.42}Pu_{0.58}O_{2+\delta}$, referred hereinafter as Pu42 and Pu58, respectively, was outlined by Markin and Street [17] with the aid of evacuated sealed quartz capillaries. The BCC superlattice reflections were not reported at low temperatures, although the composition of Pu58 falls into the stability field of BCC + FCC according to both Sari et al. [11] and Dean et al. [15]. The study of Dean et al. [15] further gave evidence for the stability of a rhombohedral phase within the range of $0.6 < Pu/(Pu + U) < 0.9$ at ambient temperature. The same study [15] provided a detailed mapping of high-temperature phase relations in Pu76 performed with the aid of evacuated sealed quartz capillaries. The high-temperature part of the diagram of Dean et al. [15] suggested the existence of the triple point of BCC(2) + FCC(1) + FCC(2) at ~840 K and the existence of the BCC(2) + FCC and FCC(1) + FCC(2) loops developing from the triple point to higher temperatures. The rhombohedral phase was observed immediately below the triple point [15]. Tight constraints to the shape and size of the immiscibility region within the range of $0.14 \leq Pu/(Pu + U) \leq 0.62$ were provided in an in-situ X-ray diffraction study of Belin et al. [18], where samples with the compositions of Pu14, Pu24, Pu35, Pu46, Pu54, and Pu62 were heated in He + 5 % H_2 + 10 ppm H_2O atmosphere to achieve sub-stoichiometric O/M ratios and then cooled down to ambient temperature. On cooling, all samples, except Pu14, entered a two-phase field. As in the study of Markin and Street [17], the BCC reflections were not observed by Belin et al. [18], although according to the diagram of Sari et al. [11], BCC should be present at least at Pu54 and Pu62. Belin et al. [18] attributed the absence of the BCC superstructure peaks to an insufficient resolution of XRD data achievable within the in-situ setup. The closing temperature of the FCC(1) + FCC(2) gap was studied with differential thermal analysis (DTA) by Koizumi and Nakamura [19] (at Pu22 and Pu24), Kato et al. [20] and Komeno et al. [21] (at Pu30), Sari et al. [11] (at Pu58, Pu80, Pu95, Pu100), and with the aid of HT-XRD by Vauchy et al. [22] (at Pu28 and Pu45), Dean et al. [15] (at Pu76) and Boivineau [12] at Pu100. Recently, Vauchy et al. [23] have detected the FCC(1) + FCC(2) = FCC transformation in Pu30, Pu45, and Pu100 with differential scanning calorimetry (DSC). All these data show that both the gap closing temperature and the width of the miscibility gap increase with the Pu/(Pu + U) ratio. The synthesis of available data also shows that the uncertainty in the closing temperature increases at higher Pu/(Pu + U) ratios, e.g., the measured temperatures for Pu100 in the studies of Sari et al. [11] and Vauchy et al. [23] are about 150 K lower than in the study of Boivineau [12].

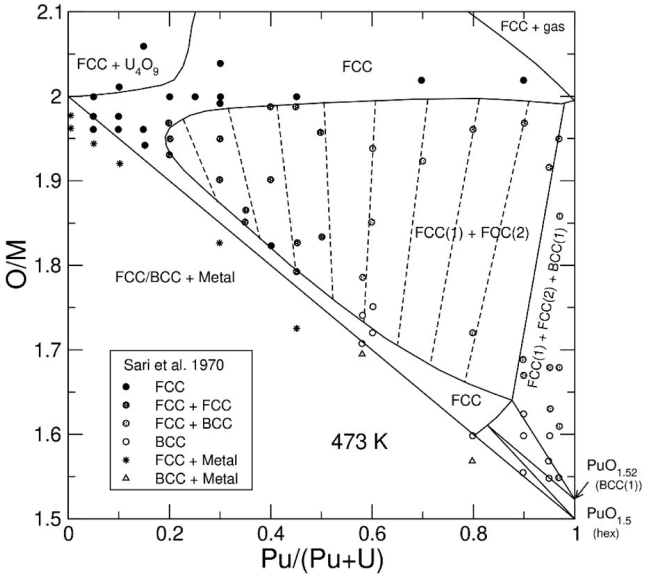

Fig. 2. Phase relations in the UO_2–$PuO_{1.5}$–PuO_2 system at 473 K assessed with CALPHAD method [6]. The diagram is redrawn from Guéneau et al. [6] as an O/M vs, $Pu/(Pu + U)$ plot. The experimental data are from Sari et al. [11].

Concluding the Sections 1.1 and 1.2, we emphasize questions that remain to be clarified:

1) The high-temperature termination of BCC in $PuO_{1.5}$–PuO_2 is uncertain. The study of Besmann [13] located it at 1400 K ($O/M \sim 1.65$) and outlined two FCC + BCC loops developing at both sides of the termination point. However, the loop at $1.62 < O/M < 1.65$ outlined in [13] was not detected in the study of Chéreau et al. [24] performed at 1373 K. The diagram of Guéneau [6] provided a compromise description of all experimental data suggesting that the loop at $1.62 < O/M < 1.65$ closes in the very vicinity of the BCC termination point. However, if the data points within the interval of $1.62 < O/M < 1.65$ would be attributed to the BCC single-phase field, the BCC field would widen and expand to higher temperatures.
2) The phase relations in $PuO_{1.5}$–PuO_2 at low temperatures are also uncertain. It is generally accepted that there are two different BCC phases often referred to as "1.52" and "1.61". It remains unclear how these two phases are related to each other crystallographically and thermodynamically. The "1.52" phase is assumed to co-exist with the hexagonal β-Pu_2O_3 down to 298 K. However, the experimental study of Haschke et al. [25] at $O/M = 1.59$ and $T < 558$ K revealed a three-phase assemblage of β-Pu_2O_3 + α-Pu_2O_3 + PuO_2, where both β-Pu_2O_3 and α-Pu_2O_3 had the same composition of $O/M = 1.5$. If the co-existence of β-Pu_2O_3 and α-Pu_2O_3 is extrapolated down to 298 K and both β-Pu_2O_3 and α-Pu_2O_3 have the same $O/M = 1.5$, then one of these phases should become unstable. This supposition would contradict the currently accepted view that the BCC "1.52" and the hexagonal β-Pu_2O_3 phases co-exists at 298 K.
3) Truphémus et al. [16] discussed the importance of triphasic, BCC+ FCC(2) + FCC(1), domain in the ternary system and observed the triple point relationship at $Pu/(Pu + U) = 0.46$, 0.54, and 0.62. However, contrary to expectation based on the phase relationships in the binary, the lattice parameter of the BCC phase was found to be

smaller than the parameter of the low-oxygen FCC phase suggesting a non-equilibrium effect. In general, the transition from BCC + FCC to FCC(1) + FCC(2) has not been yet mapped on the ternary phase diagram depending on the temperature and composition.

4) The diagram of Guéneau [6] at 473 K (Fig. 2) suggested that the phase separation of FCC into the oxygen-rich and oxygen-poor phases involves U/Pu partitioning between the phases. It is doubtful that the partitioning could occur at this low temperature considering slow cation diffusion. If the partitioning is precluded in the thermodynamic modelling, could the shape of the miscibility gap be still predicted consistently with the experiment?

The present study aims at providing plausible solutions to the problems mentioned above with the aid of a thermodynamic assessment.

2. Methods

Before giving a detailed description of thermodynamic models for the relevant phases we wish to describe conceptual difference between the modelling tools used here and in previous studies. Generally, two types of models have been used before, the associate model [26,27] and the sublattice model (also referred to as the Compound Energy Formalism, CEF) [28,6]. The latter model was implemented in the CALPHAD assessment of Guéneau [6] to describe the FCC phase. The study of Guéneau [6] included also "1.61" and "1.52" BCC phases and reproduced accurately phase relations in PuO_2–$PuO_{1.5}$. However, the U/Pu mixing was not included in the description of "1.61" and "1.52" phases. Consequently, the coexistence of FCC and BCC was not studied within the ternary system. The recent study of Vinograd et al. [29] used a hybrid approach to model the phase separation in FCC, in which the excess Gibbs free of mixing was modelled using associates, while the configurational entropy was described with an ionic model like CEF. Differently from CEF, the entropy model included effects of short-range ordering (SRO) in the oxygen sublattice. Simultaneously, the ionic model with SRO was found useful for the description of the lattice parameter variations of the exsolved FCC phases along the miscibility gap. In this study an improved variant of the model of Vinograd et al. [29] is applied to both FCC and BCC phases.

The motivation for using a hybrid thermodynamic approach is the following. The problem of the ionic model, i.e., of the Compound Energy Formalism, is the automatic generation of a variety of charge non-neutral endmembers, the properties of which are difficult to parameterise. The other drawback is the assumption of random mixing within sublattices, which in the case of O-anions and vacancies generates too much entropy. The use of charge-neutral associates as endmembers solves the first problem, but not the second one, because in the standard associate model the entropy description is oversimplified, i.e., the associates are treated as molecules that mix ideally within an imaginary "molecular" lattice. Particularly, in the description of mixing of vacancies and oxygen anions ordering effects should be considered, and these effects can be most conveniently treated on the level of ionic species. The solution proposed here is to describe the reference Gibbs free energy and the excess Gibbs free energy using a variant of an associate model and to describe the configurational entropy using a variant of ionic model, in which SRO is included. Consequently, the hybrid model has two levels, the level of associates and the level of ionic species. When it comes to the entropy calculation, the associates are split into their ionic constituents. Both levels are consistent; the fractions of associates and the fractions of ionic species in sublattices depend on the same set of internal parameters. Another novelty of the present model is the including of the chemical potential of O_2 into the definition of the Gibbs free energies of certain "oxidized" endmembers. These energies are thus defined as functions of T and of the partial pressure of O_2. Conveniently, this type of modelling does not require introducing a gas phase.

2.1. Thermodynamic model of the FCC and BCC phases in the PuO_2–$PuO_{1.5}$ system

The FCC and BCC phases, $PuO_{2+\delta}$, are described here with the same mathematical model; the difference is only in values of adjustable thermodynamic parameters. The model considers three endmembers: $PuO_{1.5}$, PuO_2, and $Pu_{0.25}Pu_{0.75}O_{1.625}$. The latter is introduced to describe vacancy ordering at the specific O/M ratio of 1.625, which we believe to be particularly important in the BCC solid solution. For the matter of convenience, $PuO_{1.5}$ FCC (i.e., a hypothetical compound with the structure of fluorite with disordered distribution of vacancies) is selected as a reference compound, and its Gibbs free energy is set equal to zero at all temperatures. The Gibbs free energies of the other endmembers are set equal to the Gibbs free energy effects of the chemical reactions, from which these endmembers are obtained from $PuO_{1.5}$ FCC. For example, the properties of PuO_2 and $Pu_{0.25}Pu_{0.75}O_{1.625}$ are defined as the Gibbs free energy effects of the reactions (1) and (2), respectively:

$$PuO_{1.5} + \frac{1}{4}\,O_2 = PuO_2, \tag{1}$$

$$PuO_{1.5} + \frac{1}{16}\,O_2 = Pu_{0.25}Pu_{0.75}O_{1.625}. \tag{2}$$

These reactions involve consumption of certain amounts of O_2 gas. The Gibbs free energy effect of O_2 consumption is equal to the negative of the chemical potential of O_2 times the amount n of moles of O_2 gas consumed. This energy is included into the Gibbs free energy of an endmember i, and the latter is written as Eq. (3):

$$G_i^{T,P_{O_2}} = \Delta G_i^0 - (T - T^0)\Delta S_i^0 + \Delta Cp_i^0\left(T - T^0 - T\ln\left(\frac{T}{T^0}\right)\right) - \Delta n_i \mu_{O_2}^{T,P_{O_2}}, \tag{3}$$

where ΔG_i^0, ΔS_i^0, and ΔCp_i^0 are the changes in the standard state properties of oxides due to the reactions (1, 2). The latter increments are considered as adjustable parameters. The chemical potential, $\mu_{O_2}^{T,P_{O_2}}$, at a given temperature and at a given partial pressure of O_2 is computed via Eq. (4):

$$\mu_{O_2}^{T,P_{O_2}} = \mu_{O_2}^{T,P^0} + T^0 S_{O_2}^0 + RT\ln\left(P_{O_2} / P^0\right), \tag{4}$$

where $\mu_{O_2}^{T,P^0}$ is from Dinsdale [30]. The term $T^0 S_{O_2}^0$, where $T^0 = 298.15$ K and $S_{O_2}^0 = 205.1373$ J/mol/K, is needed because of the standard state adopted in [30]. Due to Eq. (3), the Gibbs free energies of PuO_2 and $Pu_{0.25}Pu_{0.75}O_{1.625}$ endmembers depend on the chemical potential of O_2. Including the chemical potential of O_2 into the definition of the Gibbs free energies of the endmembers allows modelling of phase equilibria as functions of T and P_{O_2}, avoiding an explicit description of the gas phase.

The reference Gibbs free energy is modelled with Eq. (5):

$$G^{ref} = \sum_i x_i G_i^{T,P_{O_2}}, \tag{5}$$

where the endmember fractions, x_i, are defined along the following procedure. First, a disordered solid solution is built of c moles of PuO_2 and $1 - c$ moles of $PuO_{1.5}$. Then r moles of PuO_2 and $3r$ moles of $PuO_{1.5}$ are allowed to react with each other, forming $4r$ moles of the ordered endmember $Pu_{0.25}Pu_{0.75}O_{1.625}$. The fractions of $PuO_{1.5}$, PuO_2, and $Pu_{0.25}Pu_{0.75}O_{1.625}$, become $x_1 = 1 - c - 3r$, $x_2 = c - r$, and $x_3 = 4r$, respectively, as visualised in Fig. 3. The variables c and r determine the extent of reactions 1, 2) and, thus, the oxidation state. Their equilibrium values are computed via the minimization of the Gibbs free energy of mixing of a phase at a given temperature and at a given partial pressure of oxygen.

The description of the configurational entropy in fluorite-type oxides requires a special effort because of vacancy ordering. When vacancies

are inserted into a lattice filled by O^{-2} anions, the relatively positive charges of the former repel each other [31,32]. Because of this repulsion, the vacancy/oxygen distribution becomes ordered either on a local, or on a long-range scale. Both short-range and long-range ordering (SRO/LRO) affect the configurational entropy of the solid solution by limiting the fraction of oxygen lattice junctions which could be occupied by a vacancy and could be involved in the mixing process. Effectively, each vacancy creates an imaginary sphere about itself into which another vacancy cannot penetrate (Fig. S1). The forbidden space, i.e., the fraction of sites, where a vacancy could not occur, increases with the vacancy concentration, while the fraction of sites available for O/V mixing decreases. In the limiting case of the complete SRO the fractions of sites available for mixing, t, becomes equal to the fraction of vacancies, v, i.e., the vacancies become fully locked within the available space, and the configurational entropy is zero. On the other hand, when the concentration of vacancies is small, e.g., in the vicinity of PuO_2, almost every lattice junction is available for O/V mixing. In the case of a complete SRO, the difference between SRO and LRO is subtle. It depends on how regularly the forbidden junctions are distributed within the anion lattice. Here, we postulate that the states of the complete SRO and LRO are achieved in fluorite-like phases exactly at the composition of $PuO_{1.5}$, i.e., when the number of vacancies per 2 mol of O-sites approaches 0.5, and the mole fraction of vacancies is ¼. At this state, the O/V distribution is fully ordered, i.e., the vacancies are locked within ¼ of oxygen lattice sites, while the other ¾ of sites are forbidden for vacancies and, thus, are solely occupied by oxygen anions. In the case of BCC, this ordered state is thought to comply with the $Ia\bar{3}$ structure of $PuO_{1.5}$. In the case of FCC, LRO is formally absent, and the $PuO_{1.5}$ endmember is assumed to be built of different $Ia\bar{3}$ domains in anti-phase relationship to each other. Its configurational entropy is still considered to be zero. To obtain a continuous entropy equation joining the zero points at the compositions of $PuO_{1.5}$ and PuO_2, we define the number of sites (per 2.0 mol of O-sites) over which vacancies are allowed to be mixed with O-anions as $t = 2 - 1.5(1 - c)$. The concentration of vacancies within the allowed fraction of lattice junctions is then $p = v/t = 0.5(1 - c)/t$, and the configurational entropy of O/V in the solid solution is given by Eq. (6)

$$S^{conf}_{OV(dis)} = -Rt(p\ln p + (1-p)\ln(1-p)). \quad (6)$$

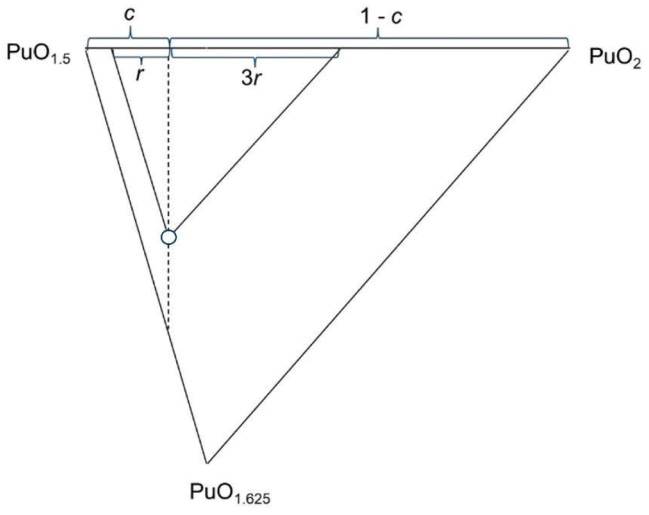

Fig. 3. The composition space of the ternary solid solution $PuO_{1.5}$–$Pu_{0.25}Pu_{0.75}O_{1.625}$–$PuO_2$. The circle represents the composition. The fraction of $Pu_{0.25}Pu_{0.75}O_{1.625}$ is equal to a $4r$ interval measured along the $PuO_{1.5}$–PuO_2 binary. The fractions of PuO_2 and $PuO_{1.5}$ are given by $c - r$ and by $1 - c - 3r$, respectively. The maximum fraction of the ordered endmember is obtained at $c = 0.25$ and $r = 0.25$.

This function takes zero values at $PuO_{1.5}$ and PuO_2 and achieves a maximum at $c \sim 0.4$ ($O/M \sim 1.7$). (See Fig. S4 for $q = 0$).

Eq. (6) corresponds to the case, where the fraction of the ordered endmember, $Pu_{0.25}Pu_{0.75}O_{1.625}$, is zero. This case is thought to be relevant at temperatures above ~1000 K. The ordered endmember, $Pu_{0.25}Pu_{0.75}O_{1.625}$, is introduced to model the effect of ordering of vacancies at the specific $O/M = 1.625$ ($\delta = -0.375$), which is thought to take place at lower temperatures. The existence of a special type of ordering at $O/M = 1.625$ was discussed by Sari et al. [7] with a reference to Mulford, who was a contributor to the 79th IAEA report [7]. Sari et al. [7] described Mulford's model with the notation "64 – 16 + 4" meaning that the vacant sublattice of bixbyite consisting of 16 sites is filled with four extra oxygen anions, which are randomised over these 16 sites. The problem of the Mulford's model is that it does not explain why this composition is special. To overcome this problem, we propose a different model, in which the extra oxygen anions introduced on top of $O/M = 1.5$ are short-range ordered within the vacant sublattice and are effectively locked (contributing zero configurational entropy) when their fraction within the vacant sublattice becomes equal ¼, i.e., when $O/M = 1.625$. The driving force of this ordering is thought to be the mutual repulsion of the extra oxygen anions, which have a negative charge relative to the neutral charge of the empty sublattice (Fig. S2). The ordered distribution of extra oxygen atoms within the empty sublattice of BCC is thus thought to be analogous to the ordered distribution of vacancies in the $PuO_{1.5}$ endmember of FCC. To emulate the effect of this additional SRO onto the entropy, we introduce four extra imaginary sublattices "1", "2_1", "2_2" and "2_3", and require that in the fully ordered "1.625" state ($c = 0.25$ and $r = 0.25$) the first sublattice is fully occupied by oxygen, while the other three contain equal fractions of vacancies (Fig. 4 and Fig. S3). Alternatively, the absence of the oxygen-oxygen avoidance corresponds to the equal distribution of the extra oxygen anions within the four sublattices. The four-sublattice model can be conveniently mapped onto the ternary solid solution model with the endmembers $PuO_{1.5}$, PuO_2 and $Pu_{0.25}Pu_{0.75}O_{1.625}$, where all endmembers have fully ordered O/V distribution. This equivalence is important because the four-sublattice model provides a convenient tool to evaluate the configurational entropy, on the other hand, the ternary model, i.e., the associate model, is very convenient for evaluating the excess Gibbs free energy of mixing. In the ternary model the fully ordered state is achieved when the fraction of the $Pu_{0.25}Pu_{0.75}O_{1.625}$ endmember is maximized, e.g., $4r = 1$, $c = 0.25$. The equivalence between the associate and sublattice models is established by linking the fraction of the ordered endmember in the ternary model, and the fractions of vacancies within the four sublattices to the same order parameter q. The value of q is set proportionally to the fraction of the ordered endmember, i.e., $q = r/c$, when $c \le 0.25$, and $q = 3r/(1 - c)$, when $c > 0.25$. The vacancy fractions in the sublattices "1", "2_1", "2_2", and "2_3" are computed as functions of q as follows. In the ordered case, the total amount of vacancies per 2 mol of O sites is still equal to $0.5(1 - c)$, but this quantity splits into two parts, $0.125(1 - c_1)$ and $0.375(1 - c_2)$, where $c_1 = c(1 + 3q) = c + 3r$ and $c_2 = c(1 - q) = c - r$. In Figure S3 the sublattice fractional occupancies are shown for the cases of $q = 0$, $q = 0.5$ and $q = 1.0$. For convenience, we increase the size of the system 4 times, i.e., to 8 mol of oxygen sites, and consider one sublattice containing $0.5(1 - c_1)$ vacancies per 2 mol of oxygen sites and another three sublattices containing $0.5(1 - c_2)$ vacancies per 2 mol of oxygen sites each. To make the four-sublattice model consistent with Eqn. 6 and with the concept of vacancy-vacancy avoidance, we require that the vacancies can occupy not more than ¼ of oxygen sites available within a sublattice, thus, when their fraction approaches ¼, the remaining ¾ of sites are considered forbidden for O/V mixing. On the other hand, when the fraction of vacancies approaches zero, they are allowed to be randomised with O-anions over all (2 mol) of oxygen sites available within a sublattice. Consequently, the allowed fractions of sites available for O/V mixing become $t_1 = 2 - 1.5(1 - c_1)$ and $t_2 = 2 - 1.5(1 - c_2)$, in the sublattices "1" and "2", respectively, while the fractions of forbidden sites are $1.5(1 -$

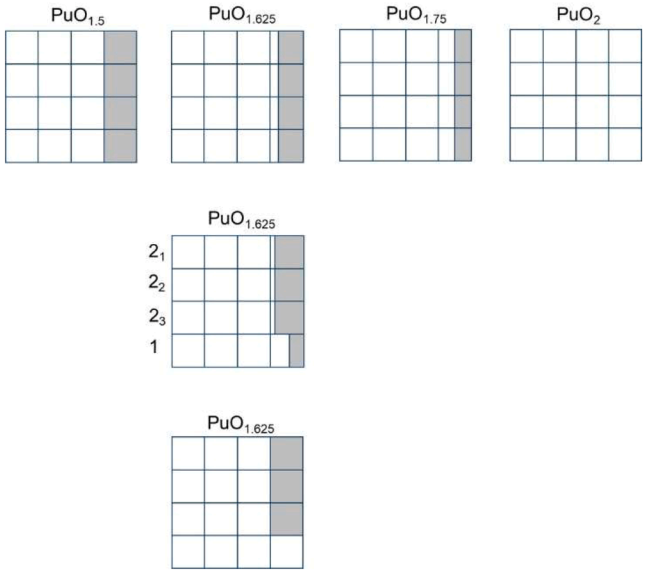

Fig. 4. The distribution of vacancies (grey) in BCC/FCC consistent with two types of SRO. The upper horizontal row illustrates the vacancy distribution at high-to-intermediate temperatures that is affected by vacancy-vacancy avoidance but is not yet perturbed by ordering at the $PuO_{1.625}$ composition. The vacancies are allowed to occupy not more than a quarter of the sites of the oxygen lattice. The limiting case of $PuO_{1.5}$ complies with the BCC-type long-range order leading to the formation of an "empty sublattice". The vertical row at $PuO_{1.625}$ illustrates an additional type of ordering that is thought to occur at low-to-intermediate temperatures within the empty sublattice. The distribution of extra oxygen anions within this sublattice is thought to be affected by oxygen-oxygen avoidance. When the mole fraction of extra oxygen atoms within the empty sublattice is equal 0.25, as in $PuO_{1.625}$, the O/V distribution could become fully ordered. The degree of order is thought to increase at lower temperatures. Thermodynamically, the effect is modelled by introducing four sublattices ("1", "2_1", "2_2" and "2_3"), none of which complies with the empty sublattice of BCC. The model is described in further details in Supplementary materials (Fig. S1-S5).

c_1) and $1.5(1-c_2)$, respectively. In Fig. S3 the forbidden fractions of sites are marked by red crosses. The concentrations of vacancies within the allowed fractions of sites become $p_1 = 0.5(1-c_1)/t_1$ and $p_2 = 0.5(1-c_2)/t_2$, and the configurational entropy of O/V within the ordered solid solution (scaled to 2 oxygen sites) takes the form

$$S_{OV}^{conf} = -0.25Rt_1(p_1\ln p_1 + (1-p_1)\ln(1-p_1)) - 0.75Rt_2(p_2\ln p_2 + (1-p_2)\ln(1-p_2)). \quad (7)$$

This function converges with Eqn. (6) at $r = 0$ ($q = 0$) and achieves a deep minimum when $c = 0.25$ and $r = 0.25$ ($q = 1$) (see Fig. S4 in Supplementary materials).

The excess Gibbs free energy of mixing in the ternary solid solution can be conveniently modelled with Equation 8

$$G^{excess} = \sum_{j\neq i} x_i x_j \left(x_i W_{iji}^g + x_j W_{ijj}^g\right), \quad (8)$$

where W_{ijk}^g are the binary Margules parameters, which are further expanded as $W_{ijk}^g = W_{ijk}^h - TW_{ijk}^s$. In the dilute limits ($c = 1$ and $c = 0$) the excess Gibbs free energy must be the same both in the disordered ($q = 0$) and in the ordered ($q = 1$) cases. To fulfil this constraint, a certain relationship between W_{ijk}^g must be satisfied. When the indices 1, 2, and 3 stand for $PuO_{1.5}$ and PuO_2 and $Pu_{0.25}Pu_{0.75}O_{1.625}$, respectively, this relationship requires $W_{131}^g = 0.25\ W_{121}^g$ and $W_{322}^g = 0.75\ W_{122}^g$ (Fig. S5). There are no such constraints on W_{133}^g and W_{323}^g, but, clearly, $W_{133}^g = W_{131}^g$ and $W_{323}^g = W_{322}^g$ are the reasonable initial assumptions to be tried in a fitting procedure.

The Gibbs free energy of mixing of an FCC or a BCC solid solution at a given set of T and P_{O_2}, is described with Eq. (9)

$$G^{mix} = G^{ref} + G^{excess} - TS_{ord}^{conf}. \quad (9)$$

Note that in Eqns. 7 and 9, the configurational entropy is fully due to the O/V disorder. Pu^{+3}/Pu^{+4} disorder is assumed not to contribute to the entropy; the electron distribution is thought to immediately adjust to any change in the O/V distribution, finding a unique ordered state. This assumption might not hold true, however, at close-to-stoichiometry conditions, where the concentrations of vacancies and Pu^{+3} cations become so small that these species cannot "find" each other and, thus, are distributed independently. Thus, it is expected that the present entropy model becomes less accurate when O/M closely approaches 2.0.

2.2. Thermodynamic model of the FCC and BCC phases in the UO_2–PuO_2–$PuO_{1.5}$ system

An extension of the $PuO_{1.5}$–$Pu_{0.25}Pu_{0.75}O_{1.625}$–$PuO_2$ model to the UO_2–$PuO_{1.5}$–PuO_2 system requires defining two new endmembers: UO_2 and $U_{0.25}Pu_{0.75}O_{1.625}$. The model becomes quinary. We chose UO_2 FCC as the second reference compound. Thus, the Gibbs free energies of the UO_2 and $PuO_{1.5}$ endmembers in the quinary fluorite model are set to zero at all temperatures. The Gibbs free energies of $U_{0.25}Pu_{0.75}O_{1.625}$ endmembers in FCC and BCC are defined via the reaction given in Equation (10)

$$\frac{1}{4}UO_2 + \frac{3}{4}PuO_{1.5} = U_{0.25}Pu_{0.75}O_{1.625}, \quad (10)$$

where the left-hand side comprises the reference endmembers. The endmember fractions, x_i, are defined as follows. First, a completely reduced solid solution is built as a mixture of z moles of $PuO_{1.5}$ and $1-z$ moles of UO_2. Then a fraction cz of $PuO_{1.5}$ is converted into PuO_2, and a fraction $(1-c)z$ of $PuO_{1.5}$ is left as $PuO_{1.5}$. Then, rz moles of PuO_2 and $3rz$ moles of $PuO_{1.5}$ are allowed to react with each other forming $4rz$ moles of $Pu_{0.25}Pu_{0.75}O_{1.625}$ endmember. Further, the fraction $3d$ of the remaining quantity $(1-c-3r)z$ of $PuO_{1.5}$ and a fraction d of the remaining quantity of UO_2 are allowed to react together, forming $4d$ moles of the $U_{0.25}Pu_{0.75}O_{1.625}$ endmember. The final fractions of $PuO_{1.5}$, PuO_2, $Pu_{0.25}Pu_{0.75}O_{1.625}$, $U_{0.25}Pu_{0.75}O_{1.625}$, and UO_2 (see also Table S1) become $x_1 = (1-c-3r)z - 3d$, $x_2 = (c-r)z$, $x_3 = 4rz$, $x_4 = 4d$, and $x_5 = 1 - z - d$, respectively, and the reference Gibbs free energy is computed with Eqn. 5 counting all endmembers in the quinary. To reduce the number of unknown parameters, the configurational entropy and the excess free energy equations in the quinary model are defined in analogy with the ternary model by combining endmembers with the same O/M ratios, i.e., the fractions UO_2 and PuO_2 are combined forming the endmember MO_2, while the fractions $Pu_{0.25}Pu_{0.75}O_{1.625}$ and $U_{0.25}Pu_{0.75}O_{1.625}$ are summed up together forming the endmember $M_{0.25}Pu_{0.75}O_{1.625}$. With this simplification, the main properties of the ternary model are retained. The fraction of MO_2 is designated y and is counted as the sum of the fractions of PuO_2 and UO_2 in the quinary as $y = x_2 + x_5$. The fraction of $M_{0.25}Pu_{0.75}O_{1.625}$ is designated $4u$ and is counted as $4u = x_3 + x_4$. The order parameter is defined as $q = u/y$, when $y \leq 0.25$ and as $q = 3u/(1-y)$, when $y > 0.25$. The fractions of vacancies in the sublattices "1" and "2" become $0.5(1-y_1)$ and $0.5(1-y_2)$, respectively, where $y_1 = y(1+3q)$ and $y_2 = y(1-q)$. The concentrations of vacancies within the fractions of sites allowed for O/V mixing within the sublattices become $p_1 = 0.5(1-y_1)/t_1$ and $p_2 = 0.5(1-y_2)/t_2$, where $t_1 = 2 - 1.5(1-y_1)$ and $t_2 = 2 - 1.5(1-y_2)$, respectively. With the modified equations for p_1, p_2, t_1, and t_2, Eqn. 7 is retained. We note, however, that Eqn. 7 evaluates only the configurational entropy due to O/V mixing. In the quinary model a contribution due to the mixing between Pu^{+4} and U^{+4} over the M sites in MO_2 and $M_{0.25}Pu_{0.75}O_{1.625}$ must be added. Under the assumption of regular mixing, this extra term

is given by Eq. (11):

$$S_{\mathrm{M}}^{\mathrm{conf}} = -yR(n_2 \ln n_2 + (1-n_2)\ln(1-n_2)) - uR(n_3 \ln n_3 + (1-n_3)\ln(1-n_3)), \quad (11)$$

where $n_2 = x_2 / (x_2 + x_5)$ and $n_3 = x_3 / (x_3 + x_4)$.

The excess enthalpy in the quinary model contains the pseudo-ternary mixing term (the analogue of Eqn. 8) and two additional Margules terms related to the excess interaction between UO_2 and PuO_2 and between $Pu_{0.25}Pu_{0.75}O_{1.625}$ and $U_{0.25}Pu_{0.75}O_{1.625}$. A combination of these terms gives Eq. (12):

$$G^{\mathrm{excess}} = \sum_{j \neq i} X_i X_j \left(X_i W_{ji}^{g} + X_j W_{ij}^{g} \right) + y n_1 (1-n_1) W_{\mathrm{U,Pu}} + u n_2 (1-n_2) W_{\mathrm{U,Pu}}. \quad (12)$$

The mole fractions of $PuO_{1.5}$, MO_2, and $M_{0.25}Pu_{0.75}O_{1.625}$ endmembers contributing to the ternary term are given as $X_1 = 1 - y - 4u$, $X_2 = y$, and $X_3 = 4u$, respectively. $W_{\mathrm{U,Pu}}$ is designated as the parameter A5 in Table S3. The Gibbs free energy of mixing of FCC or BCC is described with Eq. (13)

$$G^{\mathrm{mix}} = G^{\mathrm{ref}} + G^{\mathrm{excess}} - T\left(S_{\mathrm{OV}}^{\mathrm{conf}} + S_{\mathrm{M}}^{\mathrm{conf}} \right). \quad (13)$$

2.3. Extension of the FCC model to $\delta > 0$

Although the description of the UO_2–PuO_2–$PuO_{1.5}$ system does not require states with $\delta > 0$, it is convenient to have a model of FCC that is also applicable to the UO_3–UO_2–PuO_2–$PuO_{1.5}$ system. Particularly, such a model could be used for fitting ΔG_{O2} vs. O/M data, when the interval of measured values extends to $O/M > 2.0$. The extension to $\delta > 0$ requires little effort. Indeed, when $\delta > 0$, the reduced endmembers $PuO_{1.5}$, $Pu_{0.25}Pu_{0.75}O_{1.625}$, and $U_{0.25}Pu_{0.75}O_{1.625}$ become redundant. Thus, the states $\delta > 0$ can be modelled with three endmembers: UO_2, PuO_2 and $UO_{2.5}$. Within the $\delta > 0$ domain, the endmember fractions are set as follows. First, a stoichiometric solid solution is defined as a mixture of z moles of PuO_2 and $1 - z$ moles of UO_2. Then a fraction b of UO_2 is oxidized into $UO_{2.5}$ and the final fractions of UO_2, PuO_2, and $UO_{2.5}$ become $1 - z - b$, z, and b, respectively. The excess Gibbs energy of mixing is modelled with Eqn. 8. Following the previous modelling [29], we assume that the fluorite solid solution exists only over the interval $-0.5 \leq \delta \leq 0.33$, thus, the oxygen interstitials are allowed to occupy only $^1/_3$ of the available interstitial sites. The fraction of O-interstitials within the available sites is thus $n_1 = 3b/2$, and the entropy of Oi/Vi in the oxidized domain is modelled with Eq. (14):

$$S_{\mathrm{OiVi}}^{\mathrm{conf}} = -R \Big/ 3(n_1 \ln n_1 + (1-n_1)\ln(1-n_1)). \quad (14)$$

Pu^{+4} and U^{+4} are assumed to be mixed ideally over $1 - b$ sites, while U^{+5} cations are assumed not to contribute to the configurational entropy. The distribution of U^{+5} over M sites is thought to be fully determined by the distribution of O-interstitials over the interstitial sites. Thus, the entropy of cations is modelled with Equation 15:

$$S_{\mathrm{M}}^{\mathrm{conf}} = -R(1-b)(n_4 \ln n_4 + (1-n_4)\ln(1-n_4)), \quad (15)$$

where $n_4 = z/(1-b)$. The solid solution over the interval of $-0.5 \leq \delta \leq 0.33$ is modelled by combining the models for $\delta \leq 0$ and $\delta \geq 0$ as overlapping domains.

2.4. Modelling of the rhombohedral phase

The rhombohedral M_7O_{12} phase ($O/M = 1.714$) is modelled here as a regular binary solid solution of two endmembers $U_{3/7}Pu_{4/7}O_{12/7}$ and $Pu_{3/7}Pu_{4/7}O_{12/7}$. The excess Gibbs energy of mixing is described with Eq. (16):

$$G^{\mathrm{excess}} = \frac{3}{7} n_5 (1-n_5) W_{\mathrm{U,Pu}}, \quad (16)$$

where $n_5 = 7(1-z)/3$ is the mole fraction of $U_{3/7}Pu_{4/7}O_{12/7}$, and $W_{\mathrm{U,Pu}}$ is the same as in Eqn. 12. The entropy of mixing of U^{+4} and Pu^{+4} over 3/7 of M sites is described with Eq. (17):

$$S_{\mathrm{M}}^{\mathrm{conf}} = -\frac{3}{7} R(n_5 \ln n_5 + (1-n_5)\ln(1-n_5)). \quad (17)$$

2.5. Ion-packing model for the lattice parameter

Several studies have shown that the lattice parameters of pure UO_2 and PuO_2 and of various fluorite solid solutions, e.g., lanthanide- and actinide-doped UO_2, could be successfully modelled with ion-packing models [29,33–37]. This study follows the approach developed in [29,34,37], which is based on the following relationship between the lattice parameter, a, and the sum of the average radii of cations, $\langle R_{\mathrm{C}} \rangle$, and anions, $\langle R_{\mathrm{A}} \rangle$, given in Eq. (18):

$$a = \frac{4}{\sqrt{3}} (\langle R_{\mathrm{C}} \rangle + \langle R_{\mathrm{A}} \rangle). \quad (18)$$

Eqn. 18 assumes that cations and anions touch each other along the main diagonal of the cubic cell as hard spheres. An overlap of anion spheres along [001] is allowed in the present model. See [35] and [36] for alternative parameterization models of the lattice parameter. The average radii are computed from Shannon's ionic radii [38] and from fractions of cations and anions appearing in a structural formula. This approach is applied here to develop equations for the lattice parameters of FCC, BCC and $R\bar{3}$ phases. Importantly, when the cation and anion fractions are computed from the output of the thermodynamic model, the lattice parameter of a given phase becomes a function of the thermodynamic parameters defining the equilibrium, namely, the temperature, the oxygen partial pressure and the total Pu/(U+Pu) ratio.

The main effort in the lattice parameter modelling is to compute cation and anion fractions consistently with the thermodynamic output. Similarly to the thermodynamic model, the ion-packing model benefits from the concept of associates that can be appropriately split into ionic species. Particularly, it appears easier to describe the variation of the lattice parameter in the $PuO_{1.5}$–PuO_2 binary at the ionic level, while the effect of the $PuO_{1.625}$ endmember can be more conveniently considered at the level of mixing of associates. The effect of U^{+4} is taken into account by replacing Pu^{+4} cation by a mixture of U^{+4} and Pu^{+4} cations in a defined proportion. Importantly, the ion-packing model benefits greatly from the concept of vacancy-vacancy avoidance introduced in the thermodynamic section. This ordering translates into a restriction requiring the cation species to have only three coordination numbers, 8, 7 and 6.

Practically, the lattice parameters of FCC and BCC phases are calculated as follows. PuO_2 and UO_2 contribute Pu^{+4} and U^{+4} as 8-fold coordinated cations, while the $PuO_{1.5}$ (FCC or BCC) brings about Pu^{+3} in the 6-fold coordination. Here we consider a simplified structural model of a $PuO_{1.5}$ endmember, in which the vacancies are arranged over a BCC sublattice within the simple cubic lattice of oxygen sites in fluorite. In such a model all Pu^{+3} cations are 6-fold coordinated. In the ordered endmembers, $Pu_{0.25}Pu_{0.75}O_{1.625}$ and $U_{0.25}Pu_{0.75}O_{1.625}$, the average coordination number of cations is 6.5. Assuming that only 7- and 6-fold coordination numbers contribute to this average value, and that the largest cation, Pu^{+3}, prefers the 7-fold coordination, the structural formulas of the ordered endmembers are written $\{Pu^{+4}_{0.25}Pu^{+3}_{0.25}\}[Pu^{+3}_{0.5}]O_{1.625}$ and $\{U^{+4}_{0.25}Pu^{+3}_{0.25}\}[Pu^{+3}_{0.5}]O_{1.625}$, where the curly and square brackets embrace 6- and 7-fold cations, respectively. The average fraction of vacancies is given as $v = (0.5x_1 + 0.375x_3 + 0.375x_4)/2$, and the average fraction of O-anions is $1 - v$. Consequently, the average radius of an anion is counted as $\langle R_{\mathrm{A}} \rangle = R_{\mathrm{V}} v + R_{\mathrm{O}}(1-v)$. Then we note that the coexistence of 8- and 6-fold

cations within the same lattice should cause the appearance of a certain fraction of 7-fold cations. The fractions of 8-, 7-, and 6-fold cations that occur due to the mixing of PuO_2, UO_2, and $PuO_{1.5}$ (that are not consumed within the ordered endmembers) are counted under the assumption that vacancies, which are brought to the lattice due to $PuO_{1.5}$, are arranged over a BCC sublattice within the simple cubic lattice of oxygen sites. In such a model, the M site is surrounded by 6 oxygen anions and by 2 oxygen sites that are partially filled with vacancies. The average vacancy concentration in the latter sites is m, $m = x_1/(x_1+x_2+x_5)$, and the 8-, 7-, and 6-fold coordinated cations occur with the fractions $(1-m)^2$, $2m(1-m)$, and m^2, respectively. The endmember fractions and fractions of cations contributing to the average cation radius in FCC or BCC are given in Tables S1 and S2.

The pseudo-cubic lattice parameter of the rhombohedral $M_3Pu_4O_{12}$ phase, where M = {Pu^{+4}, U^{+4}} is calculated referring to the structural model of $Zr_3Y_4O_{12}$ δ-phase derived by Bogicevic et al. [31] from atomistic simulations. According to the latter, the larger cation, Y^{+3}, occupies a 7-fold site, while Zr^{+4} is both in 7- and in 6-fold coordination in the proportion of 2/3 and 1/3, respectively. The coordination numbers of M^{+4} and Pu^{+3} cations are assigned similarly to those of Zr^{+4} and Y^{+3}, while the fraction of U^{+4} in the M site is calculated $7(1-z)/3$, where z = Pu/(Pu + U). The average radius of an anion in $M_3Pu_4O_{12}$ is counted as $\langle R_A \rangle = \frac{1}{7}R_V + \frac{6}{7}R_O$.

The radius of O^{-2} is set 1.374 Å as in [34,37,29]. The latter studies have shown that the cubic lattice parameter of fluorite materials can be successfully modelled under the assumption that a vacancy has a defined radius, which is significantly larger than the ionic radius of O^{-2}. For example, in the study of lanthanide-doped UO_2 [37], the value of 1.541 Å was used. This value was initially tried here; however, we noticed that the data for the pure $PuO_{1.5}$–PuO_2 system requires a significantly smaller effective radius of the vacancy of ~1.460 Å. This suggested that the radius of a vacancy should be made dependent on the type of metal cation. Indeed, the simple interpolation via Equation 19

$$R_V = zR_{V(Pu)} + (1-z)R_{V(U)}, \quad (19)$$

where $R_{V(Pu)}$ = 1.460 Å and $R_{V(U)}$ = 1.541 Å, was found to fit the data well. The radii of cations are adopted from [29] with slight modifications (Table S2). Eqn. 19 predicts a positive deviation of the lattice parameters of fully reduced FCC and BCC phases from the Vegard law. The positive deviation occurs because in the vicinity of $PuO_{1.5}$, the lattice parameter elevates over the Vegard law consistently with Eqn. 19, however, when Pu/(Pu + U) approaches 0, this effect vanishes, as there are no vacancies left. The positive deviation fits well with the data of Sari et al. [11] and Dean et al. [15]. It is important to mention that the experimental BCC lattice parameter should be divided by 2 to be compared with the present model. The lattice parameter of the $R\bar{3}$ phase could be compared to the model prediction only when the structure is refined in the pseudo face-centred setting [39].

The thermal expansion of FCC, BCC, and $R\bar{3}$ is modelled here with the equation given by Kato et al. [40] for MOX, which considers effects of variable Pu/(Pu + U) and O/M ratios. However, the application of this equation at high O/M values gives inconsistent results when compared, for example, with the data of Markin and Street [17] for Pu42 and Pu58. The simulation study of Porto et al. [41] confirmed the equation of Kato et al. [40] for stoichiometric samples, but suggested that it exaggerates the effect of O/M. According to the results of Porto et al. [41], the effect of O/M is negligible at temperatures below 2000 K. Similar conclusions have been met in experimental studies of MOX [23], and other actinide dioxide systems [42,43]. Thus, we have chosen to use the equation of Kato et al. [40] with the O/M correction switched off. The equation of Martin [44] for UO_2 fluorite without a correction for the Pu/(Pu + U) ratio was also tested giving very similar results.

2.6. Fitting strategy

The starting idea in the fitting of phase relations in $PuO_{1.5}$–PuO_2 is that the FCC and BCC phases converge to the same FCC phase above a certain temperature, which is assumed to be 1800 K. The main thermodynamic difference between BCC and FCC is thought to be associated with a stronger ordering of anions in BCC at $O/M \sim 1.50$ and $O/M \sim 1.625$. The effect of the ordering at $O/M \sim 1.50$ on the Gibbs free energy of BCC is considered by setting different values for ΔG_i^0 and ΔS_i^0 parameters of $PuO_{1.5}$ and PuO_2 in BCC and FCC. The effect of ordering in BCC at $O/M \sim 1.625$ is emulated by making the ΔG_i^0 parameter of $Pu_{0.25}Pu_{0.75}O_{1.625}$ in BCC to be significantly more negative relatively to that in FCC. Because BCC and FCC are considered to be the same phase above 1800 K, we assume that the Margules interaction parameters are the same in both phases, and that the free energy differences between all the endmembers in BCC and FCC vanish at ~ 1800 K. The latter assumption was used initially to constrain the values of ΔG_i^0 and ΔS_i^0 parameters of $PuO_{1.5}$ and PuO_2 in BCC and FCC but was not followed in the end. To assure that BCC phase does not appear above 1800 K due to positive ΔS_i^0 parameters, BCC was excluded from equilibrium calculations above 1800 K. The initial values for the parameters of the FCC phase were taken from the study of Vinograd et al. [29]. The Margules parameters were adjusted to give a good representation of the ΔG_{O2} vs. O/M data of Besmann [13] within the temperature range of 1273 – 1610 K (see Fig. S6). This strategy permitted to make a rather good fit to the shapes of the BCC + FCC and FCC(1) + FCC(2) miscibility gaps. Simultaneously, we noted that the strong ordering in BCC at $O/M \sim 1.625$ causes a miscibility gap within the BCC phase at low temperatures, such that a phase with the composition of ~1.625 coexists with another phase with the composition of ~1.50. This BCC(1) + BCC(2) gap closes at about 700 K. The prediction of two BCC phases consistently with the experiment confirmed the assumption of a strong ordering effects at $O/M \sim 1.625$. Further we introduced a stochiometric compound with $O/M = 1.5$ to emulate the hexagonal β-Pu_2O_3 and tuned its ΔG_i^0 and ΔS_i^0 parameters such that the two-phase field, β-Pu_2O_3 + BCC(2), cuts the top of the BCC miscibility gap at ~670 K. Further, by slightly tuning the Margules parameters we could closely match the temperature of the triple point and the closing temperature of the FCC(1) + FCC(2) gap from Boivineau [12]. The constraints of $W^g_{131} = 0.25\ W^g_{121}$ and $W^g_{322} = 0.75\ W^g_{122}$ were kept in the fitting. The enthalpic parameters W^h_{133} and W^h_{323} were set to be ~8 % smaller that W^h_{131} and W^h_{322}.

The fitting to data for UO_2–$PuO_{1.5}$–PuO_2 was performed under the assumption that the Pu/(Pu + U) ratio is the same in FCC, BCC and $R\bar{3}$ phases and is equal to the total Pu/(Pu + U) ratio in the system (kinetic arguments in favour of this assumption are discussed in Section 2.2). The hexagonal phase was excluded upon a consideration that U/(Pu + U) ratio in this phase must be very small and that the formation of this phase from U-rich BCC should be kinetically hindered. The ΔG_i^0 and ΔS_i^0 parameters of the $U_{0.25}Pu_{0.75}O_{1.625}$ and UO_2 endmembers in BCC were adjusted to provide the best description of the high-temperature XRD data of Dean et al. [15], Belin et al. [18], Vauchy et al. [23], and Markin and Street [17]. Particularly, the ΔG_i^0 and ΔS_i^0 of the UO_2 endmember were fixed such that the BCC is stable at ambient temperature at Pu/(Pu + U) > 0.36, while the BCC(2) + FCC(1) + FCC(2) triple point occurs at Pu76 at 840 K consistently with the study of Dean et al. [15]. The Gibbs free energies of $U_{3/7}Pu_{4/7}O_{12/7}$ of $Pu_{3/7}Pu_{4/7}O_{12/7}$ endmembers of $R\bar{3}$ were set such that this phase becomes unstable at Pu/(Pu + U) > 0.95, while its stability at Pu/(Pu + U) = 0.62 is limited by the interval of 298 K < T < 750 K.

The assessed thermodynamic parameters are given in Table S3 (Supplementary materials).

3. Results

3.1. The assessed phase relations in $PuO_{1.5}$–PuO_2

The phase relations in $PuO_{1.5}$–PuO_2 were calculated as a function of T and $\Delta G_{O_2} = RT\ln(P_{O_2}/P^0)$, which were varied within the intervals 273 K < T < 2173 K and –1500 kJ/mol < ΔG_{O_2} < 0 kJ/mol with the steps of 25 K and 1 kJ/mol, respectively. The total Gibbs free energy minimum was computed at each pair of ΔG_{O_2} and T with a FORTRAN code. The lattice parameters were calculated for the stable BCC and/or FCC phases with the aid of the ion-packing model. Fig. 5 plots the temperature as a function of O/M, while Fig. 6 shows the same phase relations by plotting the equilibrium cubic lattice parameters of FCC and BCC as a function of temperature. The BCC(1) and BCC(2) phases are considered here to belong to the same solid solution phase. They become distinguishable because of the miscibility gap developing within BCC. α-Pu_2O_3 (BCC(1)) is predicted to be the most stable phase at 298.15 K at O/M = 1.5, while β-Pu_2O_3 is predicted stable at T > 550 K. The BCC + FCC(1) + FCC(2) triple point is located at 890 K, in a reasonable agreement with the data of Boivineau [12] (Fig. 6). The BCC + FCC loop is in good agreement with the data of Chéreau et al. [24] and Besmann [13]. However, the BCC/FCC transition at $PuO_{1.5}$ is placed here about 300 K higher in temperature relative to the diagrams of Besmann [13] and Guéneau et al. [6]. The higher termination temperature is a consequence of a reinterpretation of the ΔG_{O_2} vs. O/M data of Besmann [13] at 1400 K. In our interpretation, the two-phase FCC + BCC field at the low oxygen side does not exist, while the field of stability of BCC expands to lower O/M values until it is cut by the two-phase β-Pu_2O_3 + BCC field. The wider field of the single-phase BCC at 1400 K requires its expansion to higher temperatures. A small inflexion in the ΔG_{O_2} vs. O/M data at 1610 K (Fig. S6) seems to support our interpretation, as it can be attributed to the transition from β-Pu_2O_3 + BCC to the single-phase BCC field.

The assessed differences in the thermodynamic data of PuO_2 fluorite and β-Pu_2O_3 (Table S3) ΔG^0 = −216.5 kJ/mol, ΔS^0 = −17.18 J/K/mol, compare well with the values of −200.6 ± 6 kJ/mol, and −15.4 ± 0.6 J/K/mol given in the review of Chartier et al. [45]. The ΔC_p^0=14.5 J/K/mol adopted here is close to the average heat capacity difference of 18.6 J/K/mol between PuO_2 and β-Pu_2O_3 over the interval of 300 – 1600 K computed using $C_p(T)$ equations provided by Konings et al. [46].

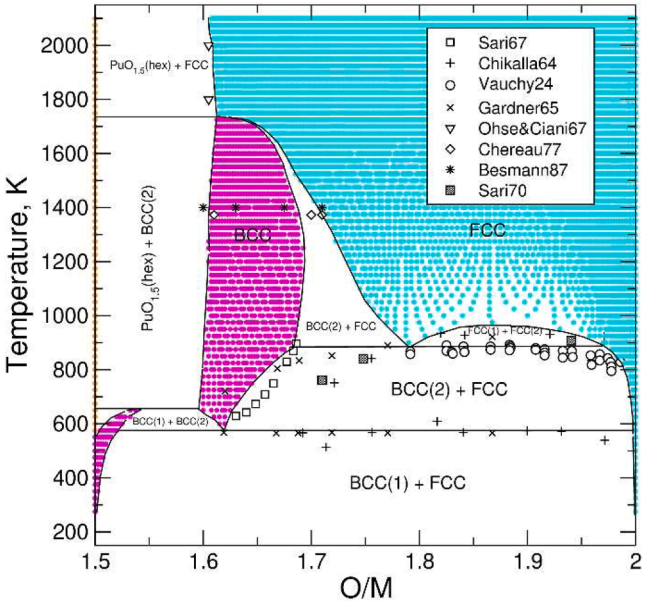

Fig. 5. The assessed phase relations in the $PuO_{1.5}$–PuO_2 system within the interval of 1.5 < O/M < 2.0. The experimental data are from Sari et al. [7,11], Chikalla et al. [9], Gardner et al. [10], Vauchy et al. [23], Chéreau et al. [24], Ohse and Ciani [14], and Besmann [13]. Blue and pink circles correspond to FCC and BCC phases, respectively. Each circle represents a result of total Gibbs free energy minimization constrained by values of ΔG_{O_2} and T. The parameters were varied within the intervals of 273 K < T < 2173 K and –1500 kJ/mol < ΔG_{O_2} < 0 kJ/mol with the steps of 25 K and 1 kJ/mol, respectively.

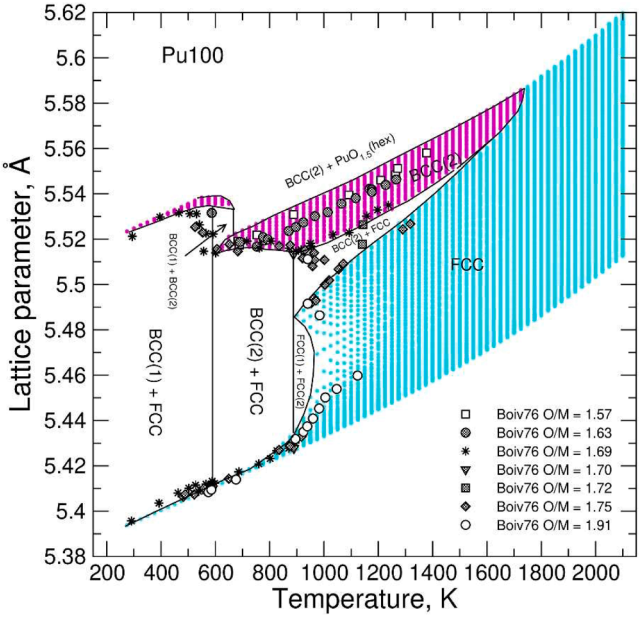

Fig. 6. Equilibrium cubic lattice parameters of FCC and BCC in the $PuO_{1.5}$–PuO_2 system plotted as functions of the temperature. Each blue (FCC) or pink (BCC) circle corresponds to a pair of ΔG_{O_2} and T. The experimental data are from Boivineau [12].

3.2. The assessed phase relations in UO_2–$PuO_{1.5}$–PuO_2

The phase relations in UO_2–$PuO_{1.5}$–PuO_2 are very sensitive to the ΔG_i^0 and ΔS_i^0 parameters of the UO_2 BCC endmember, which are set here 2.0 kJ/mol and 0.0 J/K/mol, respectively. These values fit the triple point of BCC + FCC(2) + FCC(1) in Pu76 at ~840 K, consistently with Dean et al. [15], and constrain the stability of BCC at 298 K at Pu/(Pu + U) > 0.36, a compromise result that agrees with the data of both Dean et al. [15] and Sari et al. [11]. The results of the calculations are presented in Figs. 7–13 and Fig. S6-S10. The phase relations at Pu76 (Fig. 7) are very similar to those at Pu100 (Fig. 6). The main difference is that at Pu76 the triple point moves to about 60 K lower temperature and that the rhombohedral phase becomes stable below the triple point. Dean et al. [15] assumed this phase to be M_7O_{12} (O/M = 1.714), however, they noted that its composition appeared to be closer to 1.70. Here, this phase is modelled as M_7O_{12} (O/M = 1.714), and its pseudo-cubic parameter is predicted to be about 0.01 Å smaller relative to the values measured by Dean et al. [15]. This deviation is consistent with the more reduced composition of the $R\bar{3}$ phase estimated by Dean et al. [15]. Fig. 8 illustrates the phase relations within the range of Pu62 – Pu14 consistently with compositions of the samples studied by Belin et al. [18]. With the decrease in Pu/(Pu + U) ratio from 0.62 to 0.46 the triple point drops down from ~760 K to ~580 K, and at Pu/(Pu + U) = 0.35 BCC is unstable. The closing temperature of the FCC(1) + FCC(2) gap decreases from ~850 K at Pu/(Pu + U) = 0.62 to ~460 K at Pu/(Pu + U) = 0.14. The $R\bar{3}$ phase is predicted to be stable at Pu62 (Fig. 8 (a)), consistently with the result of Dean et al. [15], however, the XRD data of Belin et al. [18] for Pu62 seems to be inconsistent with the presence of $R\bar{3}$. The lattice parameter of the low-oxygen phase is ~0.015 Å smaller than the predicted values of the pseudo-cubic parameter of $R\bar{3}$. Thus, the simulations suggest that the formation of $R\bar{3}$ was either suppressed at

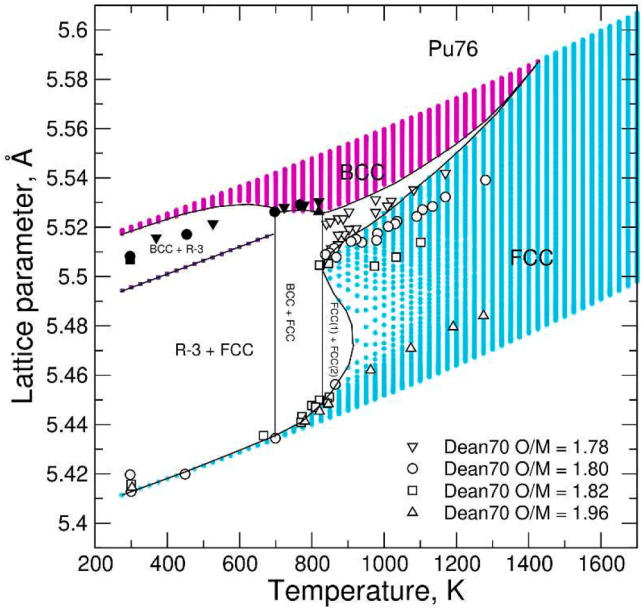

Fig. 7. Assessed BCC/FCC equilibria in the UO_2–$PuO_{1.5}$–PuO_2 system as compared to the experimental data of Dean et al. [15] for Pu76. White and black symbols correspond to cubic and rhombohedral phases, respectively.

Pu62 or this phase was quickly oxidized and transformed into FCC. The latter explanation is plausible due to the prompt oxidation of hypo-stoichiometric phases even at low temperatures [47].

Although BCC was not observed in [17] and [18], the lattice parameter data of Belin et al. [18] for Pu62, Pu54, Pu46 (Fig. 8 (a-c)), as well as the data of Markin and Street [17] for Pu42 and Pu58 (Fig. S7 (a, b)) do not contradict the presence of a BCC phase at these compositions. The low-temperature tails of the data of Markin and Street [17] for Pu42 and Pu58 (Fig. S7 (a)) fit well with the BCC + FCC equilibrium. The shape of the miscibility gap in Pu35 (Fig. 8 (d)) is consistent with the instability of BCC at this composition. In the case of Pu24, the gap closing is predicted at ~600 K, consistently with the experiment, however, the assessed width of the gap is much wider (Fig. 8 (e)). It appears that in the case of Pu24, the experimental conditions were not optimal for observing the full width of the gap, possibly, because the *O/M* fraction of the sample when it entered the two-phase field was already close to 2.0. In the case of Pu14 the model predicts immiscibility below 460 K (Fig. 8 (f)). The data of Belin et al. [18] do not show an immiscibility at this composition, apparently, because the *O/M* ratio of the sample has reached the value of ~2.0 before entering the gap. Further tests to the accuracy of the present model are provided by DSC and HT-XRD data on Pu30 and Pu45 constraining the closing temperature of the FCC(2) + FCC(1) gap. The predicted diagrams compare favourably with available data (Fig. 9 (a, b)).

Fig. 10 shows the shape of the miscibility gap in *O/M* vs. Pu/(Pu + U) plot at 473 K together with the data of Sari et al. [11]. The experimental data correspond to samples with the composition in the range of $0 \leq Pu/(Pu + U) \leq 0.97$, either synthesized at 1773 – 2273 K and then slowly cooled to room temperature or annealed at 473 K and then slowly cooled. We tentatively assume that these samples were equilibrated at ~473 K. The model predicts the FCC to BCC transition at Pu/(Pu + U) ~ 0.4 in reasonable agreement with the experiment. The rhombohedral phase is predicted to be stable at $0.57 < Pu/(Pu + U) < 0.96$, in agreement with Dean et al. [15]. This phase was not observed in the study of Sari et al. [11], however. The same phase relations are depicted in Fig. 11 as the lattice parameter vs. Pu/(Pu + U) diagram together with the experimental data from Sari et al. [11] and from Dean et al. [15]. Although the data of Dean et al. [15] are claimed to represent room temperature, we speculate that, due to kinetic constraints, the realistic equilibration temperature was a bit higher. Thus, these data are plotted at 473 K. The thermodynamic calculations align well with the data. Figures S8, S9 and S10 illustrate the variations of phase relations within the interval of $273\ K < T < 873\ K$.

Knowing the equilibrium temperature and the lattice parameter allows one to determine the corresponding *O/M* value and/or the ΔG_{O_2}. This, in turn, permits comparing data of different types obtained in different experimental studies. For example, in Fig. 12 the lattice parameter data of Belin et al. [18] for Pu46 are plotted in a *T* vs. *O/M* diagram. This allows for a direct comparison with the DSC data of Vauchy et al. [22] for Pu45. Clearly, the two datasets agree very well with each other suggesting that the two phases that occur due to the phase separation are in the thermodynamic equilibrium. This inter-phase equilibrium does not imply, however, that both phases occur in equilibrium with the gas phase. Figures 13(a) and 13(b) plot ΔG_{O_2} vs. *O/M* for the samples Pu46 and Pu45, respectively, annealed at different cooling rates. The data of Belin et al. [18] (Fig. 13(a)) obtained at the cooling rate of 3 K/s, between two temperature steps separated by 50 K, strongly deviate from the equilibrium with the gas phase, while the data of Vauchy et al. [22] obtained at much slower rate of 0.005 K/s closely approach the state of the thermodynamic equilibrium (Fig. 13(b)). The phase separation occurs in the former, but not in the latter case. This shows that the oxygen potential set in equilibrium experiments of Vauchy et al. [22] was higher than that required for observing the gap, while the strong disequilibrium with the gas phase occurring in the experiments of Belin et al. [18] allowed the samples to reach the reducing conditions that are consistent with the gap.

4. Discussion

The developed models of BCC and FCC solutions explain the main features of the $PuO_{1.5}$ – PuO_2 diagram [6] (Fig. 1), providing simultaneously a slightly different interpretation of the relationship between the observed phases in detail. Progress is achieved by explicitly considering the effects of vacancy ordering, which are thought to be responsible for structural and thermodynamic distinction between FCC and BCC. At temperatures above ~1750 K, the only solid solution phase is FCC fluorite. The vacancy distribution in fluorite is thought to be affected by short-range ordering even at high temperatures. This SRO, driven by the vacancy-vacancy repulsion, is thought to become particularly strong at *O/M* ~ 1.5 leading presumably to the formation of BCC-like ordered domains in anti-phase orientation with each other. At about 1750 K, $Ia\bar{3}$ domains with a certain orientation win, and the BCC phase forms. Due to the change in symmetry the Gibbs free energy of the $PuO_{1.5}$ endmember in BCC becomes slightly more negative relatively to the same endmember in FCC. BCC and FCC phases coexist along a single two-phase field, which becomes wider with the decrease in temperature (Fig. 5). The mixing properties of both FCC and BCC solid solutions at high temperatures are determined by positive configurational entropy due to the O/V disorder and by the excess Gibbs free energy, which is composed of large positive excess enthalpy and entropy terms. At high temperatures, the latter contributions compensate for each other, favoring miscibility, but, at about 950 K, and *O/M* ~ 1.85 the FCC phase separates into FCC(1) and FCC(2). This immiscibility does not affect BCC, because the *O/M* range of BCC does not exceed 1.71. At ~890 K, FCC(2) becomes unstable relative to BCC and FCC(1), and below this temperature BCC coexists with oxygen-rich FCC(1). At lower temperatures the phase relations become more complex because of an additional SRO effect occurring at *O/M* ~ 1.625. Due to this effect, the Gibbs free energy decreases particularly strongly at *O/M* ~ 1.625, and the excess Gibbs free energy is more closely described as consisting of two hills elevating at both sides of a valley centered at *O/M* = 1.625 (Fig. S5). This peculiar shape of the excess free energy is responsible for the phase separation effect developing in BCC below ~700 K (Fig. 5). This ordering has little effect on FCC, because the composition of FCC in equilibrium with BCC is shifted to larger *O/M*

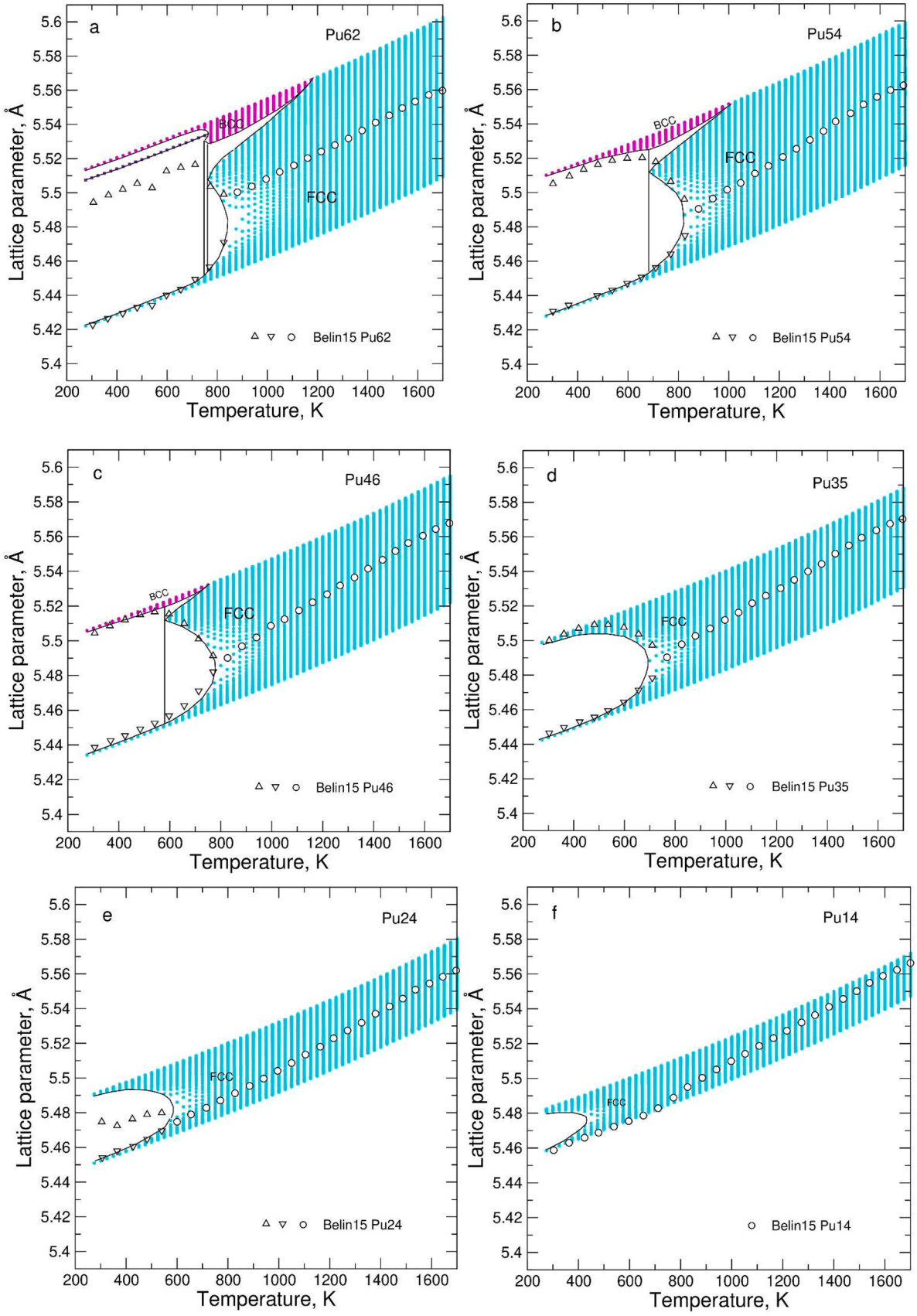

Fig. 8. a-f. Assessed BCC/FCC equilibrium in the UO_2–$PuO_{1.5}$–PuO_2 system as compared to the experimental data of Belin et al. [18]. The closing temperature of the FCC(1) + FCC(2) gap decreases from Pu62 (a) to Pu14 (f).

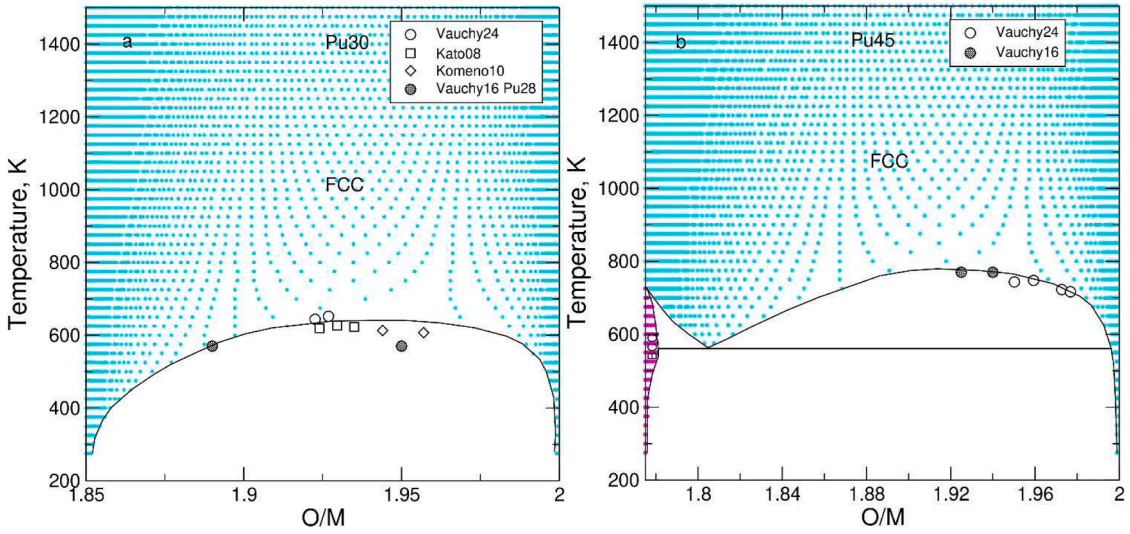

Fig. 9. a, b. Predicted phase relations at Pu30 (a) and Pu45 (b) in comparison with available experimental data of Vauchy et al. [23,22], Kato et al. [20], and Komeno et al. [21].

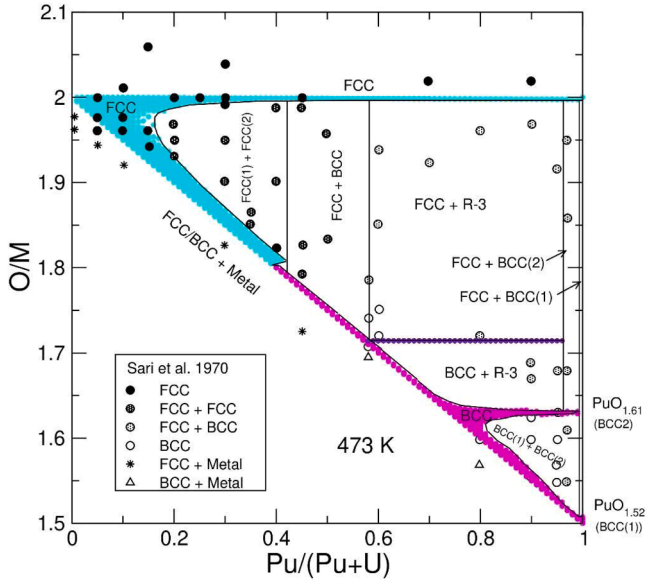

Fig. 10. Predicted phase relations in the system UO_2–$PuO_{1.5}$–PuO_2 at 473 K. The experimental data are from Sari et al. [11].

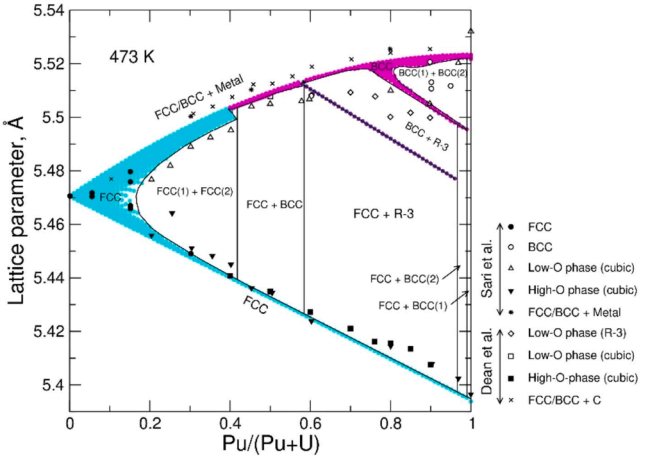

Fig. 11. Predicted variation of the equilibrium cubic lattice parameter in the UO_2–$PuO_{1.5}$–PuO_2 system at 473 K. The experimental data are from Sari et al. [11] and Dean et al. [15]. Lattice parameters are plotted at 298 K, i.e., the effect of thermal expansion is not included.

values. Within the range of 700 K – 600 K two miscibility gaps, BCC(1) + BCC(2) and BCC(2) + FCC(1), exist simultaneously, but at ~ 600 K the free energy of the BCC(2) becomes unstable relative to the mixture of BCC (1) and FCC(1), and at $T < 600$ K BCC(1) coexists with a nearly stoichiometric FCC(1). The phase relations at $1.5 < O/M < 1.625$ are further affected by the stabilization of the hexagonal β-Pu_2O_3, which has a larger entropy and a larger standard Gibbs free energy than the $PuO_{1.5}$ end-member of BCC. Thus, BCC(1) is the most stable phase at 298.15 K and at $O/M = 1.5$. β-Pu_2O_3 forms at about 550 K and at 550 K $< T <$ 670 K, it coexists with BCC(1). At ~670 K, the condition for the triple point of β-Pu_2O_3 + BCC(1) + BCC(2)) is met. At higher temperatures, BCC(1) vanishes and β-Pu_2O_3 coexists with BCC(2) up to ~1750 K. The predicted diagram (Fig. 5) differs from the currently accepted model of Guéneau et al. [6] in three main aspects: 1) the stability of BCC is extended to ~300 K higher temperature; 2) "$PuO_{1.52}$" and "$PuO_{1.61}$" phases belong to the same BCC solid solution phase; 3) the hexagonal phase is stable above ~550 K.

The HT-XRD study of Boivineau [12] (Fig. 6) located the BCC + FCC (1) + FCC(2) triple point at ~940 K (see the data at $O/M = 1.91$). In our assessment, this point is shifted to about 50 K lower temperature. This is done as a compromise attempting to minimize model misfit with the results of Boivineau [12], on the one hand, and with the DTA results Sari et al. [11] and DSC results of Vauchy et al. [23], on the other hand. The problem is that Boivineau [12] located the closing of the FCC gap at ~1040 K, while the studies of Sari et al. [11] and Vauchy et al. [23] located it at about 150 K lower temperature. The disagreement between the present assessment and Boivineau [12] could be explained by noting that the experimental runs of Boivineau were done on heating, thus, the three-phase assemblage recorded at ~940 K could have equilibrated at a slightly lower temperature. Still, the location of the triple point at ~890 K contradicts the closing temperatures measured in the DSC and DTA studies of Vauchy et al. [23] and Sari et al. [11], i.e., if the gap closes at ~890 K, then the triple point should be moved to an even lower temperature. Not excluding such a solution, we propose here a different interpretation. Under the assumption that the present assessment is correct, the flat segment of the DSC data of Vauchy et al. [23] that is spreading over $1.77 < O/M < 1.92$, as well as one data point of Sari et al.

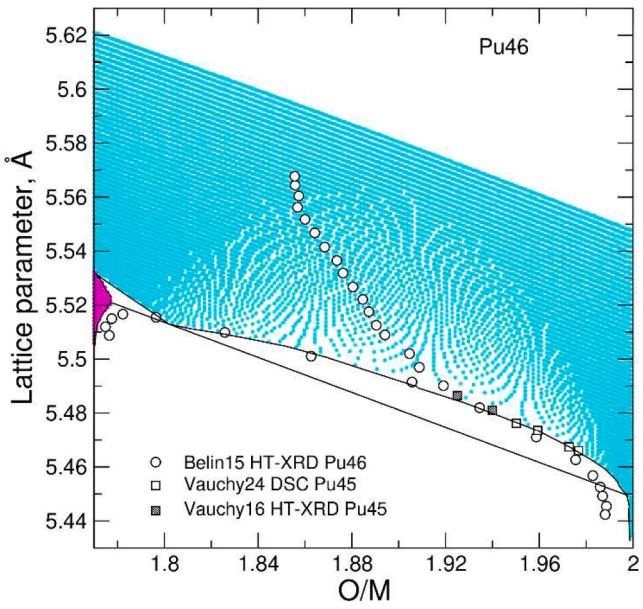

Fig. 12. Predicted phase relations at Pu46 in comparison with the experimental data of Vauchy et al. [22,23] and Belin et al. [18]. The lattice parameter data of Belin et al. [18] are converted into *O/M* values assuming that local equilibrium is achieved for each data point.

[11] at $O/M = 1.94$, (Fig. 5) are consistent with the BCC + FCC(2) = FCC (1) transformation. The data of Vauchy et al. [23] at $O/M > 1.92$ fall closely to the predicted BCC + FCC(2) = FCC transformation boundary. The data of Sari et al. [11] at ~ 1.71 and 1.74 appear to match the metastable continuation of the FCC(1) + FCC(2) loop into the BCC(2) + FCC(1) field. Clearly, this interpretation is tentative, and neither DSC, nor DTA signals contain definitive information on the nature of recorded transformations. Further experimental and modelling effort are needed to fully understand this complex part of the diagram.

The *O/M* vs. Pu/(Pu + U) plot in the ternary UO_2–$PuO_{1.5}$–PuO_2 system (Fig. 10) can be directly compared to the diagram of Guéneau et al. [6] at 473 K (Fig. 2). The main difference is that in our model the BCC phase is predicted stable not only in the $PuO_{1.5}$–PuO_2 binary, but also over a wide range of Pu/(Pu + U) values in the ternary. We also predict phase separation in BCC. The hexagonal phase is predicted stable only at $T > 550$ K; thus, it does not appear in the 473 K plot. The BCC/FCC transition is predicted at Pu/(Pu + U) ~ 0.4 in fair agreement with the diagram of Sari et al. [11]. The variations of the phase relations as functions of the composition and temperature are illustrated with Figs. 7, 8, and 11, and with Figures S7, S9 and S10. An important observation is that the phase relations in *O/M* vs. Pu/(Pu + U) and in *T* vs. *O/M* plots appear to be topologically similar. The decrease in Pu/(Pu + U) and an increase in the temperature have qualitatively similar effects on phase relations. This can be rationalized noting that both an increase in the fraction of U and an increase in the temperature stabilize solid solution phases by increasing their *TS* terms. Similarly to the phase relations in *T* vs. *O/M* diagram (Fig. 5), the BCC is separated from FCC via a BCC-FCC loop (Fig. 10 and Fig S9), while the collision of this loop with the FCC(1) + FCC(2) gap leads to the formation of the triple point. Thus, the transition from FCC to BCC in the ternary system necessarily involves the formation of the triphasic assemblage. Although the FCC + BCC assemblage is very important for explaining phase relations in *O/M* vs. Pu/(Pu + U) at Pu/(Pu + U) > 0.4, the data of Markin and Street [17] for Pu42 and Pu58 and of Belin et al. [18] for Pu46, Pu54 and Pu62 do not provide evidence for the formation of BCC at these compositions. On the other hand, modelling the latter data as FCC(1) + FCC(2) equilibrium would have resulted in a problem describing the data of Sari et al. [11] and Dean et al. [15].

The rhombohedral phase is predicted to be stable at $T < 750$ K and at $0.57 < Pu/(Pu + U) < 0.96$. According to Sari et al. [11], the hexagonal β-Pu_2O_3 exists at ambient temperatures only at Pu/(Pu + U) > 0.97. In the present assessment of UO_2–$PuO_{1.5}$–PuO_2 equilibria, this phase is excluded, however, its presence in the $PuO_{1.5}$–PuO_2 subsystem is indicated in the ternary diagrams.

Importantly, the present assessment of equilibria in UO_2–$PuO_{1.5}$–PuO_2 assumes that *no* U/Pu partitioning between different phases have occurred under the conditions of the relevant experiments. This assumption fits well with the experimentally determined cation interdiffusion coefficients that are too small at the phase

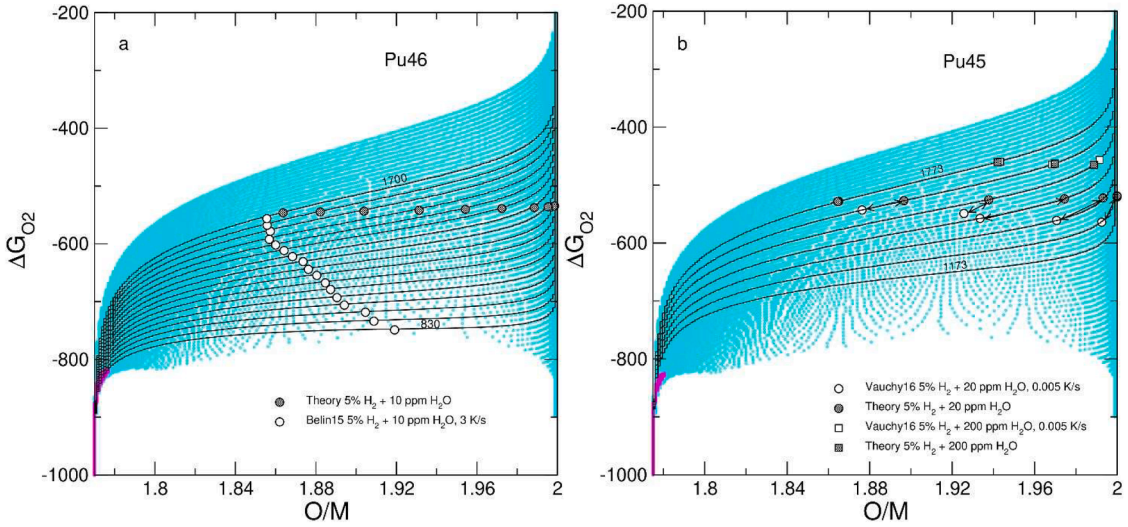

Fig. 13. Predicted phase relations at Pu46 and Pu45 in comparison with the experimental data of Belin et al. [18] (a) and Vauchy et al. [22] (b). Solid lines are the isotherms of $\Delta G_{O_2} = RTln(P_{O_2}/P^0)$ computed at thermodynamic equilibrium. Open circles correspond to *O/M* values recalculated from the lattice parameter data reported in the studies. Filled circles correspond to *O/M* values predicted at thermodynamic equilibrium with He gas containing 5 % of H_2 and *n* ppm of H_2O. The data set of Belin et al. [18] strongly deviates from the thermodynamic equilibrium with the gas, however, the low-temperature tail of the data has reached the conditions of the miscibility gap. On the contrary, the data set of Vauchy et al. [22] much closely corresponds to the thermodynamic equilibrium. The conditions of the two-phase equilibrium were not met, and the phase separation was not observed in the study. The reason for the qualitatively different results obtained by Belin et al. [18] and Vauchy et al. [22] is the difference in cooling rates, which were 3 *K/s* and 0.005 *K/s*, respectively.

separation temperatures to allow any U/Pu segregation [16,47–50]. Thus, BCC, FCC and the rhombohedral phase are assumed to have *the same* Pu/(Pu + U) ratios in all experiments selected for the assessment, and this constraint is implemented in the thermodynamic modelling. The experimental observation of the occurrence of $R\bar{3}$ within 0.6 < Pu/(Pu + U) < 0.9 interval at room temperature is consistent with the assumption of the absence of U/Pu partitioning, because, if $R\bar{3}$ is requested to have the Pu/(Pu + U) ratio equal to the total Pu/(Pu + U) in the system, it could be stable only at Pu/(Pu + U) > 4/7 (i.e., at Pu/(Pu + U) > 0.5714), as is observed. The absence of the hexagonal phase at Pu/(Pu + U) < 0.97 is also consistent with the assumption of ineffectiveness of U/Pu partitioning between different phases. The β-Pu_2O_3 phase likely can hold only a little fraction of UO_2, and, thus, its crystallization from an UO_2-rich FCC or BCC would necessarily require U/Pu partitioning and solid-state U/Pu diffusion to occur. The slowness of the latter would prevent the formation of β-Pu_2O_3 in a measurable quantity. Good fit to most of the experimental data in UO_2–$PuO_{1.5}$–PuO_2 achieved here under the applied constraint suggests that the original data represent constrained equilibria. If true unconstrained equilibrium would hold and if U/Pu partitioning between phases would be efficient, then the Pu-rich β-Pu_2O_3 could possibly appear in phase assemblages at lower Pu/(Pu + U) ratios. As most of the data considered in the present study fall within the range of 298 K < *T* < 1000 K, and as these data are fitted well with the constrained option, we assume that the U/Pu partitioning remains effectively frozen below ~1000 K. The absence (or extreme slowness) of U/Pu partitioning is consistent with a difficulty of experimental observation of triphasic assemblages [16,18]. The same Pu/(Pu + U) ratio in all phases has a consequence that the area of a triphasic assemblage on an *O/M* vs. Pu/(Pu + U) diagram must be zero.

The absence of U/Pu partitioning at experimental conditions implies that the thermodynamic assessment algorithm, when applied to such data, should have the constraint of the equal Pu/(Pu + U) ratios in the relevant phases. However, the application of the constrained model at high temperatures might be erroneous. Indeed, in the experiments of Vauchy et al. [50] well defined diffusional profiles in diffusion couples were obtained within days at ~1800 K.

The slow rates of U/Pu diffusion at ambient conditions might also be responsible for the enhanced resistivity of MOX fuel to oxidation relatively to undoped UO_2 [51–54]. The slow U/Pu partitioning would likely hinder the formation of the M_3O_8 phase at Pu-rich compositions. Indeed, the HT-XRD studies of Strach et al. [52,55] have shown that M_3O_8 can hold only a small fraction of Pu, and that the equilibrium formation of M_3O_8 from a Pu-rich MO_2 oxide involves a strong partitioning of Pu into the parent cubic phase. This partitioning would be practically precluded at ambient temperature, thus hindering the formation of M_3O_8. A similar mechanism has been recently proposed to explain the resistivity of Ln-doped UO_2 to oxidation [37].

The equilibrium calculations show that phase separation phenomena in hypo-stoichiometric MOX occur at strongly reducing conditions, i.e., at $\Delta G_{O_2} < -750$ kJ/mol (Fig. 13). These very reduced states are best achieved in experiments in sealed quartz capillaries, where the oxygen partial pressure is controlled by solid-state equilibria. In the HT-XRD experiments of Belin et al. [18] and Vauchy et al. [22], the oxygen potential in the gas phase was controlled by H_2O/H_2 equilibrium, i.e., with an inert gas containing 5 % H_2 and *n* ppm of H_2O. With this technique, it appears impossible to achieve states with $\Delta G_{O_2} < -570$ kJ/mol [22]. This is due to intrinsic impurities they contain, as well as impurities added by imperfect experimental setups (e.g., small leaks, material degassing). Consequently, it is impossible to observe the phase separation, if the thermodynamic equilibrium between the solids and the gas is maintained. This has been experimentally shown by Vauchy et al. [22] employing cooling rates of 0.005 K/s. However, during a rapid cooling of a sample in an HT-XRD experiment, i.e., with the rates of 2–3 K/s, the solid phase behaves as a quasi-closed system and thus exists at much more reducing conditions relatively to experiments that are performed close to equilibrium. The studies of Vauchy et al. [22] and Belin et al. [18] illustrate these two contrasting cases. It appears that at fast cooling rates, the solids buffer oxygen potential at values that are significantly lower relative to a value set by the gas mixture. Apparently, in such experiments strong oxygen potential gradients exist at grain boundaries. Due to these gradients the *O/M* values of the samples increase gradually in the course of the experiment as illustrated in Figs. 12 and 13.

As soon as the sample enters the gap, the prompt O/V diffusion promotes the phase separation into low- and high-oxygen phases that are in equilibrium with each other, but not with the gas phase. As the temperature decreases further, the total *O/M* ratio continues drifting to more oxidized states, as was demonstrated by Belin et al. [18]. In two-phase assemblages, this drift could be accommodated by changing fractions of low- and high-oxygen phases, and/or by an increase in *O/M* of the oxygen-poor phase relatively to a value that corresponds to perfect equilibrium. Vauchy et al. [47] have shown that at ambient temperature these two processes occur simultaneously. The relatively fast oxidation of the low-oxygen BCC (or $R\bar{3}$) phase could possibly explain more oxidized *O/M* values measured for Pu62 and Pu54 relatively to those predicted at the thermodynamic equilibrium (Fig. 8 (a, b)). The data of Truphémus et al. [16], Vigier et al. [56], and Vauchy et al. [47] indicate fast oxidation of the low-oxygen phase. It is likely that the oxidation promotes the conversion of BCC (or $R\bar{3}$) into FCC. This effect could contribute to the difficulty of identifying the presence of the BCC phase in HT-XRD experiments [18].

The present model consistently with Dean et al. [15] predicts the stability of $R\bar{3}$ within the interval of 0.57 < Pu/(Pu + U) < 0.96. The predicted lattice parameters of $R\bar{3}$ at Pu76 are at variance with the data of Dean et al. [15], showing values ~0.01 Å smaller than in the experiment. A possible explanation is that the samples of Dean et al. [15] contained a mixture of BCC and $R\bar{3}$. Indeed, Dean et al. [15] wrote that, in the experiments with *O/M* = 1.78, some X-ray diffraction patterns of $R\bar{3}$ showed superstructure lines of BCC. A possible reason for this observation might be that the equilibration of samples with *O/M* > 1.714 at low temperatures started with the crystallization of a metastable association of BCC + FCC. These phases reacted then to form the stable $R\bar{3}$, but a small fraction of BCC survived. On the other hand, when the ordered $R\bar{3}$ phase is formed, it is likely to survive at temperatures that exceed its stability domain. This could be the reason for the lower $R\bar{3}$ termination temperature predicted here relatively to the data of Dean et al. [15] for Pu76 (Fig. 7). Our assessment for Pu62 (Fig. 8 (a)) predicts the stability of $R\bar{3}$. This prediction appears at variance with the study of Belin et al. [18], where the $R\bar{3}$ phase was not observed. This disagreement could also be attributed to a difficulty in the nucleation of ordered $R\bar{3}$. The likely explanation for the low-temperature tail of the data for Pu62 is that it corresponds to the metastable FCC(2) + FCC(1) equilibrium, where the metastable oxidized FCC(2) replaces a more stable BCC.

5. Conclusions

Our assessment provides plausible solutions to the four problems in $PuO_{1.5}$–PuO_2 and UO_2–$PuO_{1.5}$–PuO_2 phase relations outlined in the Introduction:

1) The field of stability of BCC phase in $PuO_{1.5}$–PuO_2 system should be extended by about 300 K to higher temperatures as a compromise between the data of Besmann [13] and Chéreau et al. [24]. The FCC-BCC loop at the left from the BCC field is likely cut off by the field of stability of β-Pu_2O_3 + BCC.
2) The “1.52” and “1.61” phases most likely belong to the same solid solution phase and are separated from each other by a miscibility gap. The “1.52” phase does not have a fixed composition and should not be modelled as a line compound. At *T* ~ 298 the composition of the “1.52” phase decreases to ~1.50. BCC is thus the most stable

$PuO_{1.5}$ polymorph of at 298.15 K. The hexagonal phase is predicted stable only at $T > 550$ K.

3) The topology of T vs. O/M diagrams in UO_2–$PuO_{1.5}$–PuO_2 system (Fig. 10 and Fig. S9) appears to be similar to the topology of the phase diagram of the $PuO_{1.5}$–PuO_2 system (Fig. 5). The O/M ratio of BCC at the triple point is always smaller than O/M ratios of the FCC phases. With increasing temperature, the triple point moves to a higher Pu/(U + Pu) ratio. This effect is related to shrinking the gap with the temperature primarily at UO_2-rich composition.
4) Low-temperature phase relations in UO_2–$PuO_{1.5}$–PuO_2 system could be described sufficiently well under the assumption of the absence of U/Pu partitioning between FCC and BCC phases.

The predicted phase relations $PuO_{1.5}$–PuO_2 system are in a generally good agreement with the results of the CALPHAD assessment study of Guéneau et al. [6], although, the fit to experimental data is obtained here with the aid of different thermodynamic models and by implying a different thermodynamic constraint. This agreement shows that a good fit to experimental data could be achieved withdifferent thermodynamic tools. The main advantage of the developed hybrid approach is its ability to evaluate equilibrium lattice parameters of FCC and BCC phases and thus to include more experimental constraints into the assessment. Thus, further progress in thermodynamic modelling of phase relation in UO_2–$PuO_{1.5}$–PuO_2 system could be foreseen when the hybrid model is implemented into a dedicated thermodynamic software. The predicted FCC-FCC and FCC-BCC equilibria in the ternary are in good agreement with the data of Sari et al. [11], Dean et al. [15], and Vauchy et al. [22, 23] and with high-temperature tails of the data of Markin and Street [17] and Belin et al. [18] that refer to FCC(1) + FCC(2) equilibrium. However, at variance with the results of Markin and Street [17] and Belin et al. [18], our assessment attributes the low-temperature tails of the data for Pu62 – Pu42 (see Fig. 8 (a-c) and S7 (a,b)) not to FCC(1) + FCC(2), but to BCC + FCC(1) equilibrium. Further investigations are needed to support our interpretation.

The present study confirms the notion [18,22] that the phase separation phenomenon in UO_2–$PuO_{1.5}$–PuO_2 cannot be observed in equilibrium experiments where the oxygen potential is controlled by a gas mixing equipment, which does not allow achieving ΔG_{O_2} values lower than ~ –750 kJ/mol at $T \sim 900$ K. The gas mixing tools used in the studies of Belin et al. [18] and Vauchy et al. [22] allowed achieving ΔG_{O_2} values of ~ −570 kJ/mol, which are inconsistent with the gap. Although MOX synthesis studies are typically performed at $\Delta G_{O_2} > -570$ kJ/mol, the phase separation is a matter of concern, because the equilibrium with the gas is rarely achieved. Achieving the equilibrium would require cooling rates of $10^{-2} - 10^{-3}$ K/s [22].

A good agreement with most of available data UO_2–$PuO_{1.5}$–PuO_2 achieved here under the constraint of the absence of interphase U/Pu partitioning confirms indirectly the slowness of solid-state cation diffusion in fluorite-like oxides in the temperature range where the phase separation occurs. This implies that the thermodynamic assessment of low-temperature experimental data should be performed with algorithms that specifically preclude U/Pu partitioning. However, the exact temperature at which the constrained option should be switched on is still uncertain. We suggest that further modelling effort should be made to investigate the phase equilibria in UO_2–$PuO_{1.5}$–PuO_2 and in UO_3–UO_2–$PuO_{1.5}$–PuO_2 systems under both constrained and unconstrained conditions.

Despite remaining open questions, the predicted relationship between a, T, z, and O/M can be used as a convenient tool for estimating oxidation states and phase compositions of MOX samples equilibrated at $T < 1000$ K.

Funding

This research did not receive any specific grant from funding agencies in the public, commercial, or not-for-profit sectors.

CRediT authorship contribution statement

Victor L. Vinograd: Writing – original draft, Software, Methodology, Formal analysis, Data curation, Conceptualization. **Romain Vauchy:** Writing – review & editing, Formal analysis, Data curation, Conceptualization.

Declaration of competing interest

We have nothing to declare.

Acknowledgments

VV and RV thank A.A. Bukaemskiy, G. Murphy, G. Deissmann, G. Modolo and D. Bosbach for the discussion of the first variant of this MS, which helped to improve its readability and quality. The advice and support of D. Kulik, O. Fabrichnaya and M. Luchitskaia were very helpful at several stages of model development and are greatly acknowledged.

Supplementary materials

Supplementary material associated with this article can be found, in the online version, at doi:10.1016/j.jnucmat.2025.156244.

Data availability

We have shared the link to Zenodo repository that contains codes used to create the phase diagrams. The link is given in Supplementary materials.

References

[1] Y. Guérin, Fuel performance of fast spectrum oxide Fuel, Compr. Nucl. Mater. 2 (2012) 547–578.
[2] R. Vauchy, A-Ch. Robisson, F. Audubert, F. Hodaj, Ceramic processing of uranium-plutonium mixed oxide fuels $(U_{1-y}Pu_y)O_2$ with high plutonium content, Ceram. Int. 40 (2014) 10991–10999.
[3] M. Kato, S. Maeda, T. Abe, K. Asakura, Uranium oxide and MOX production, Compr. Nucl. Mater. 2 (2020) 1–34.
[4] M. Di Gennaro, A. Magni, M. Guarnieri, D. Pizzocri, L. Luzzi, C. Guéneau, P. Van Uffelen, Modelling and assessment of thermophysical properties of Am-bearing fuels for transmutation purposes in fast reactors, Prog. Nucl. Energy 185 (2025) 105698.
[5] S. Hirooka, T. Matsumoto, M. Kato, T. Sunaoshi, H. Uno, T. Yamada, Oxygen potential measurement of $(U,Pu,Am)O_{2\pm x}$ and $(U,Pu,Am,Np)O_{2\pm x}$, J. Nucl. Mater. 542 (2020) 152424.
[6] C. Guéneau, N. Dupin, B. Sundman, C. Martial, J.-C. Dumas, S. Gossé, S. Chatain, F. D. Bruycker, D. Manara, R.J.M. Konings, Thermodynamic modelling of advanced oxide and carbide nuclear fuels: description of the U–Pu–O–C systems, J. Nucl. Mater. 419 (2011) 145–167, https://doi.org/10.1016/j.jnucmat.2011.07.033.
[7] C. Sari, U. Benedict, H. Blank, Thermodynamics of Nuclear Materials, 1967, IAEA, Vienna, 1968, pp. 587–611. ISBN: 9789200400681.
[8] H.A. Wriedt, The O–Pu (oxygen–plutonium) system, Bull. Alloy Ph. Diagr. 11 (1990) 184–202, https://doi.org/10.1007/BF02841705.
[9] T.D. Chikalla, C.E. McNeilly, R.E. Skavdahl, The plutonium–oxygen system, J. Nucl. Mater. 12 (1964) 131–141, https://doi.org/10.1016/0022-3115(64)90132-1.
[10] E.R. Gardner, T.L. Markin, R.S. Street, The plutonium–oxygen phase diagram, J. Inorg. Nucl. Chem. 27 (1965) 541–551, https://doi.org/10.1016/0022-1902(65)80259-7.
[11] C. Sari, U. Benedict, H. Blank, A study of the ternary system UO_2–PuO_2–Pu_2O_3, J. Nucl. Mater. 35 (1970) 267–277, https://doi.org/10.1016/0022-3115(70)90211-4.
[12] J.-C. Boivineau, Étude par rayons X du diagramme plutonium–oxygène de la température ambiante jusqu'à 1100°C, J. Nucl. Mater. 60 (1976) 31–38, https://doi.org/10.1016/0022-3115(76)90114-8.
[13] T.M. Besmann, Phase equilibria and thermodynamics of the Pu–O system: 1400 K to 1610 K, J. Nucl. Mater. 144 (1987) 141–150, https://doi.org/10.1016/0022-3115(87)90289-3.
[14] R.W. Ohse, C. Ciani, Thermodynamics of Nuclear Materials, 1967, IAEA, Vienna, 1968, pp. 545–557.
[15] G. Dean, J.-C. Boivineau, P. Chéreau, J.-P. Marcon, Contribution to the study of the U–Pu–O system, in: Proc. 4th Int. Conf. Plutonium Actin., Nuclear Metallurgy, Santa Fe, New Mexico, USA, 1970, pp. 753–761.

[16] T. Truphémus, R.C. Belin, J.-C. Richaud, M. Reynaud, M.-A. Martinez, I. Félines, A. Arredondo, A. Miard, T. Dubois, F. Adenot, J. Rogez, Structural studies of the phase separation in the UO_2–PuO_2–Pu_2O_3 ternary system, J. Nucl. Mater. 432 (2013) 378–387, https://doi.org/10.1016/j.jnucmat.2012.07.034.

[17] T.L. Markin, R.S. Street, The uranium–plutonium–oxygen ternary phase diagram, J. Inorg. Nucl. Chem. 29 (1967) 2265–2280, https://doi.org/10.1016/0022-1902(67)80281-1.

[18] R.C. Belin, M. Strach, T. Truphémus, C. Guéneau, J.-C. Richaud, J. Rogez, In situ high temperature X-ray diffraction study of the phase equilibria in the UO_2–PuO_2–Pu_2O_3 system, J. Nucl. Mater. 465 (2015) 407–417, https://doi.org/10.1016/j.jnucmat.2015.06.034.

[19] M. Koizumi, Y. Nakamura, Phase Studies and Fuel Performance in the System Pu−U−O, Power Reactor and Nuclear Fuel Development Corporation, 1970.

[20] M. Kato, K. Morimoto, A. Komeno, S. Nakamichi, M. Kashimura, Experimental evaluation of Am and Np bearing mixed oxide fuel properties, in: Actin. Fission Prod. Partitioning Transmutat. - Tenth Inf. Exch. Meet., Organisation for Economic Cooperation and Development - Nuclear Energy Agency, Mito, Ibaraki-ken, Japan, 2008.

[21] A. Komeno, M. Kato, H. Uno, K. Takeuchi, K. Morimoto, M. Kashimura, Phase separation behaviour of $(U_{0.7}Pu_{0.3})O_{2-x}$ ($1.92<x<2.00$) based fuels containing actinides and/or lanthanides, in: IOP Conf. Ser. Mater. Sci. Eng., IOP Publishing, San-Fransisco, California, USA, 2010 012016, https://doi.org/10.1088/1757-899X/9/1/012016.

[22] R. Vauchy, R.C. Belin, A.-C. Robisson, F. Hodaj, Effect of cooling rate on achieving thermodynamic equilibrium in uranium–plutonium mixed oxides, J. Nucl. Mater. 469 (2016) 125–132, https://doi.org/10.1016/j.jnucmat.2015.11.049.

[23] R. Vauchy, S. Hirooka, Y. Horii, M. Ogasawara, T. Sunaoshi, T. Yamada, T. Tamura, T. Murakami, Uranium–plutonium–oxygen phase diagram: investigating the solvus of fluorite's exsolution, J. Nucl. Mater. 599 (2024) 155233.

[24] P. Chéreau, G. Dean, M. De Franco, P. Gerdanian, High-temperature microcalorimetric measurements of partial molar enthalpy of solution, $\Delta H(O_2)$, in plutonium+oxygen, J. Chem. Thermodyn. 9 (1977) 211–219.

[25] J.M. Haschke, L.N. Dinh, W. McLean II, The plutonium–oxygen phase diagram in the 25–900°C range: non-existence of the $PuO_{1.515}$ phase, J. Nucl. Mater. 458 (2015) 275–280, https://doi.org/10.1016/j.jnucmat.2014.12.106.

[26] T.M. Besmann, T.B. Lindemer, Chemical thermodynamic representation of <PuO2-x>and <U1-zPuzOw>, J. Nucl. Mater. 130 (1985) 489–504.

[27] R. Agarwal, B.K. Sen, V. Venugopal, Phase diagram analysis of $(U,Pu)O_{2-x}$ sub-system, J. Nucl. Mater. 385 (2009) 112–116, https://doi.org/10.1016/j.jnucmat.2008.10.017.

[28] S. Yamanaka, H. Kinoshita, K. Kurosaki, Phase relation assessment for O–Pu–U ternary system, J. Nucl. Mater. 326 (2004) 185–194, https://doi.org/10.1016/j.jnucmat.2004.01.011.015.

[29] V.L. Vinograd, A.A. Bukaemskiy, G. Deissmann, G. Modolo, A structural-thermodynamic model of the $(U_{1-z}Pu_z)O_{2+\delta}$ solid solution, MRS Adv. 9 (2024) 373–380, https://doi.org/10.1557/s43580-024-00818-z.

[30] A.T. Dinsdale, SGTE data for pure elements, Calphad 15 (4) (1991) 317–425.

[31] A. Bogicevic, C. Wolverton, G.M. Crosbie, E.B. Stechel, Defect ordering in aliovalently doped cubic zirconia from first principles, Phys. Rev. B 64 (2001) 014106.

[32] A. Bogicevic, C. Wolverton, Nature and strength of defect interactions in cubic stabilized zirconia, Phys. Rev. B 67 (2003) 024106, https://doi.org/10.1103/PhysRevB.67.024106(2003).

[33] T. Ohmichi, S. Fukushima, A. Maeda, H. Watanabe, On the relation between lattice parameter and O/M ratio for uranium dioxide-trivalent rare earth oxide solid solution, J. Nucl. Mater. 102 (1981) 40–46.

[34] A.A. Bukaemskiy, V.L. Vinograd, P.M. Kowalski, Ion distribution models for defect fluorite ZrO_2 - $AO_{1.5}$ (A=*Ln, Y*) solid solutions: I. Relationship between lattice parameter and composition, Acta Mater. 202 (2021) 99–111.

[35] R. Vauchy, S. Hirooka, M. Watanabe, M. Kato, Breaking the hard-sphere model with fluorite and antifluorite solid solutions, Sci. Rep. 13 (2023) 2217, https://doi.org/10.1038/s41598-023-29326-0.

[36] R. Vauchy, S. Hirooka, T. Murakami, Ionic radii in fluorites, Materialia 32 (2023) 101934, https://doi.org/10.1016/j.mtla.2023.101934.

[37] V.L. Vinograd, A.A. Bukaemskiy, G. Deissmann, G. Modolo, Thermodynamic model of the oxidation of *ln*-doped UO_2, Sci. Rep. 13 (2023) 17944.

[38] R. Shannon, Revised effective ionic radii and systematic studies of interatomic distances in halides and chalcogenides, Acta Cryst. A32 (1976) 751–767, https://doi.org/10.1107/S0567739476001551.

[39] L. Eyring, N.C. Baenziger, On the structure and related properties of the oxides of praseodymium, J. Appl. Phys. 33 (1962) 428–433.

[40] M. Kato, Y. Ikusawa, T. Sunaoshi, A.T. Nelson, K.J. McClellan, Thermal expansion measurement of $(U,Pu)O_{2-x}$ in oxygen partial pressure-controlled atmosphere, J. Nucl. Mater. 469 (2016) 223–227.

[41] G. Porto, J. Bouchet, D. Bathellier, J. Bodin, M. Canducci, J. Tranchida, P. Fossati, P. Martin, E. Bourasseau, Thermodynamic and thermoelastic properties of hypostoichiometric MOX fuels with molecular dynamics simulations, J. Nucl. Mater. 598 (2024) 155163.

[42] E. Epifano, Ch. Guéneau, R.C. Belin, R. Vauchy, F. Lebreton, J-Ch. Richaud, A. Joly, Ch. Valot, P.M. Martin, Insight into the Am−O phase equilibria: A thermodynamic study coupling high-temperature XRD and CALPHAD modeling, Inorg. Chem. 56 (2017) 7416–7432.

[43] R. Vauchy, A. Joly, Ch. Valot, Lattice thermal expansion of $Pu_{1-y}Am_yO_{2-x}$ plutonium–americium mixed oxides, J. Appl. Cryst. 50 (2017) 1782–1790.

[44] D.G. Martin, The thermal expansion of solid UO_2 and (U, Pu) mixed oxides – a review and recommendations, J. Nucl. Mater. 152 (1988) 94–101.

[45] By A. Chartier, L. Van Brutzel, P. Fossati, Ph. Martin, Chr. Guéneau, Thermodynamic and thermophysical properties of the actinide oxides, in: R.J. M Konings, R.E. Stoller, R. Agarwal (Eds.), Comprehensive Nuclear Materials, Second EditionComprehensive Nuclear Materials, 7, Elsevier, 2020, pp. 112–141. By, https://10.1016/B978-0-12-803581-8.11786-2.

[46] R.J.M. Konings, O. Beneš, A. Kovács, D. Manara, D. Sedmidubský, L. Gorokhov, V. S. Iorish, V. Yungman, E. Shenyavskaya, E. Osina, The thermodynamic properties of the *f*-elements and their compounds. Part 2. The lanthanide and actinide oxides, J. Phys. Chem. Ref. Data 43 (2014) 013101.

[47] R. Vauchy, A.-C. Robisson, R.C. Belin, P.M. Martin, A.C. Scheinost, F. Hodaj, Room-temperature oxidation of hypostoichiometric uranium–plutonium mixed oxides $U_{1-y}Pu_yO_{2-x}$ – A depth-selective approach, J. Nucl. Mater. 465 (2015) 349–357, https://doi.org/10.1016/j.jnucmat.2015.05.033.

[48] R. Vauchy, R.C. Belin, A.-C. Robisson, F. Hodaj, High temperature X-ray diffraction study of the kinetics of phase separation in hypostoichiometric uranium–plutonium mixed oxides, J. Eur. Ceram. Soc. 34 (2014) 2543–2551, https://doi.org/10.1016/j.jeurceramsoc.2014.02.028.

[49] R. Vauchy, S. Hirooka, T. Matsumoto, M. Kato, Cation interdiffusion in uranium–plutonium mixed oxide fuels: where are we now? Front. Nucl. Eng. 1 (2022) 1060218.

[50] R. Vauchy, T. Matsumoto, S. Hirooka, H. Uno, T. Tamura, T. Arima, Y. Inagaki, K. Idemitsu, H. Nakamura, M. Machida, T. Murakami, Uranium-plutonium-americium cation interdiffusion in polycrystalline (U, Pu, Am)$O_{2\pm x}$ mixed oxides, J. Nucl. Mater. 588 (2024) 154786.

[51] J.M. Elorrieta, D. Manara, L.J. Bonales, J.F. Vigier, O. Dieste, M. Naji, R.C. Belin, V. G. Baonza, R.J.M. Konings, J. Cobos, Raman study of the oxidation in (U, Pu)O_2 as a function of Pu content, J. Nucl. Mater. 495 (2017) 484–491.

[52] M. Strach, R.C. Belin, J.-C. Richaud, J. Rogez, High temperature X-ray diffraction study of the oxidation products and kinetics of uranium–plutonium mixed oxides, Inorg. Chem. 53 (2014) 12757–12766, https://doi.org/10.1021/ic501580x.

[53] C. Jégou, R. Caraballo, S. Peuget, D. Roudil, L. Desgranges, M. Magnin, Raman spectroscopy characterization of actinide oxides $(U_{1-y}Pu_y)O_2$: resistance to oxidation by the laser beam and examination of defects, J. Nucl. Mater. 405 (2010) 235–243.

[54] R.J. McEachern, P. Taylor, A review of the oxidation of uranium dioxide at temperatures below 400°C, J. Nucl. Mater. 254 (1998) 87–121.

[55] M. Strach, R.C. Belin, J-Ch. Richaud, J. Rogez, Biphasic MO_{2+x}−M_3O_{8-z} domain of the U−Pu−O phase diagram, Inorg. Chem. 54 (2015) 9105–9114.

[56] J-F. Vigier, M. Philippe, P.M. Martin, L. Martel, D. Prieur, A.C. Scheinost, J. Somers, Structural investigation of $(U_{0.7}Pu_{0.3})O_{2-x}$ mixed oxides, Inorg. Chem. 54 (2015) 5358–5365.